Cell Reports

Article

THBS1+ myeloid cells expand in SLD hepatocellular carcinoma and contribute to immunosuppression and unfavorable prognosis through TREM1

Graphical abstract

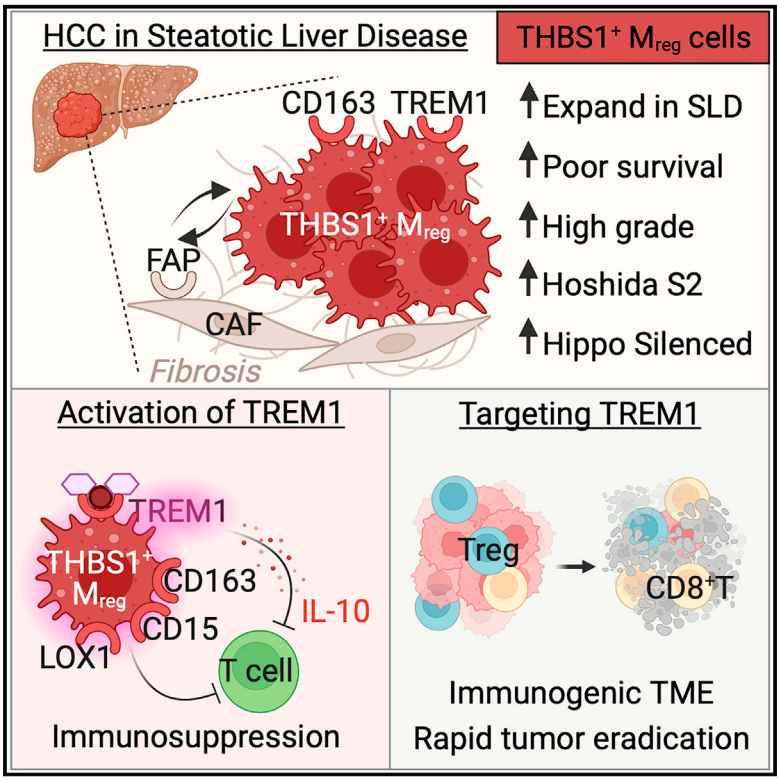

Authors

Julie Giraud, Domitille Chalopin, Eloïse Ramel, ..., Marc Derive, Macha Nikolski, Maya Saleh

Correspondence

maya.saleh@inrs.ca

In brief

Giraud et al. characterize the innate immune landscape of HCC. They identify an immunosuppressive THBS1+ myeloid population co-expressing TREM1 and CD163 that expands in the steatotic liver disease etiology of HCC and contributes to unfavorable prognosis through TREM1. TREM1 blockade elicits an immunogenic TME and rapid tumor eradication.

Highlights

- Atlas of hepatic innate immune cells from patients with HCC
- THBS1+ M_{reg} cells expand in SLD-associated HCC and populate fibrotic lesions
- TREM1 engagement potentiates immunosuppression and HCC growth *in vivo*
- THBS1+ M_{reg} density and TREM1 expression associate with HCC poor prognosis

Giraud et al., 2024, Cell Reports *43*, 113773
February 27, 2024
https://doi.org/10.1016/j.celrep.2024.113773

CellPress

Cell Reports

CellPress
OPEN ACCESS

Article

THBS1^{+} myeloid cells expand in SLD hepatocellular carcinoma and contribute to immunosuppression and unfavorable prognosis through TREM1

Julie Giraud,[1,10] Domitille Chalopin,[1,8,10] Eloïse Ramel,[1] Thomas Boyer,[1] Atika Zouine,[2] Marie-Alix Derieppe,[3] Nicolas Larmonier,[1] Olivier Adotevi,[4] Brigitte Le Bail,[5] Jean-Frédéric Blanc,[6] Christophe Laurent,[6] Laurence Chiche,[6] Marc Derive,[7] Macha Nikolski,[8] and Maya Saleh[1,9,11,*]

[1]University of Bordeaux, CNRS, ImmunoConcEpT, UMR 5164, 33000 Bordeaux, France
[2]Bordeaux University, CNRS UMS3427, INSERM US05, Flow Cytometry Facility, TransBioMed Core, 33000 Bordeaux, France
[3]University of Bordeaux Animal Facilites, 33600 Pessac, France
[4]Université Bourgogne Franche-Comté, INSERM, UMR1098, 25000 Besançon, France
[5]Bordeaux University Hospital, Division of Pathology, Pellegrin Hospital, 33000 Bordeaux, France
[6]University of Bordeaux Hospital, Division of Gastrohepatology and Oncology, Haut Leveque Hospital, 33604 Pessac, France
[7]Inotrem SA, Nancy, France
[8]University of Bordeaux, CNRS, IBGC, UMR 5095, 33000 Bordeaux, France
[9]Institut National de la Recherche Scientifique (INRS), Armand Frappier Health & Biotechnology (AFSB) Research Center, Laval, QC H7V 1B7, Canada
[10]These authors contributed equally
[11]Lead contact
*Correspondence: maya.saleh@inrs.ca
https://doi.org/10.1016/j.celrep.2024.113773

SUMMARY

Hepatocellular carcinoma (HCC) is an inflammation-associated cancer arising from viral or non-viral etiologies including steatotic liver diseases (SLDs). Expansion of immunosuppressive myeloid cells is a hallmark of inflammation and cancer, but their heterogeneity in HCC is not fully resolved and might underlie immunotherapy resistance. Here, we present a high-resolution atlas of innate immune cells from patients with HCC that unravels an SLD-associated contexture characterized by influx of inflammatory and immunosuppressive myeloid cells, including a discrete population of THBS1^{+} regulatory myeloid (M_{reg}) cells expressing monocyte- and neutrophil-affiliated genes. THBS1^{+} M_{reg} cells expand in SLD-associated HCC, populate fibrotic lesions, and are associated with poor prognosis. THBS1^{+} M_{reg} cells are CD163^{+} but distinguished from macrophages by high expression of triggering receptor expressed on myeloid cells 1 (TREM1), which contributes to their immunosuppressive activity and promotes HCC tumor growth *in vivo*. Our data support myeloid subset-targeted immunotherapies to treat HCC.

INTRODUCTION

Hepatocellular carcinoma (HCC) ranks among the most common malignancies worldwide, with a rising incidence in the Western world. Despite well-known risk factors, i.e., chronic viral infection with hepatitis B virus, primarily in Asia, and hepatitis C virus in Western countries, and steatotic liver diseases (SLDs)[1] including alcohol consumption-associated steatohepatitis and metabolic dysfunction-associated steatohepatitis (previously referred to as non-alcoholic steatohepatitis [NASH]), HCC is diagnosed late in most patients.[2] While several systemic treatments have been approved for advanced HCC, e.g., tyrosine kinase inhibitors, they provide small clinical benefit.[3] The landscape of clinical trials for HCC has shifted to immunotherapy, with the approval of immune checkpoint inhibitors (ICIs), in first-line treatment (atezolizumab/bevacizumab and durvalumab/tremelimumab).[3,4] However, ~75% of patients do not respond to these treatments for unclear reasons.[5] A previous meta-analysis of three randomized phase 3 clinical trials administering ICI to patients with advanced HCC showed a superior efficacy of immunotherapies in virally infected patients compared to NASH-affected patients with HCC,[6] pointing to the tumor microenvironment (TME) as an important determinant of therapeutic success and highlighting the urgent need to identify theranostic immune biomarkers for patient stratification and to develop additional immunotherapies.

Myeloid cells are a main immune infiltrate in several solid tumors and are considered an impediment to all cancer therapeutic modalities, particularly immunotherapy. Modulating their recruitment, differentiation, or functions is being actively pursued as a therapeutic option.[7] However, their indiscriminate depletion has failed to improve cancer patient overall survival, indicating that a better characterization of myeloid subsets is required for a targeted approach. Myeloid cells encompass

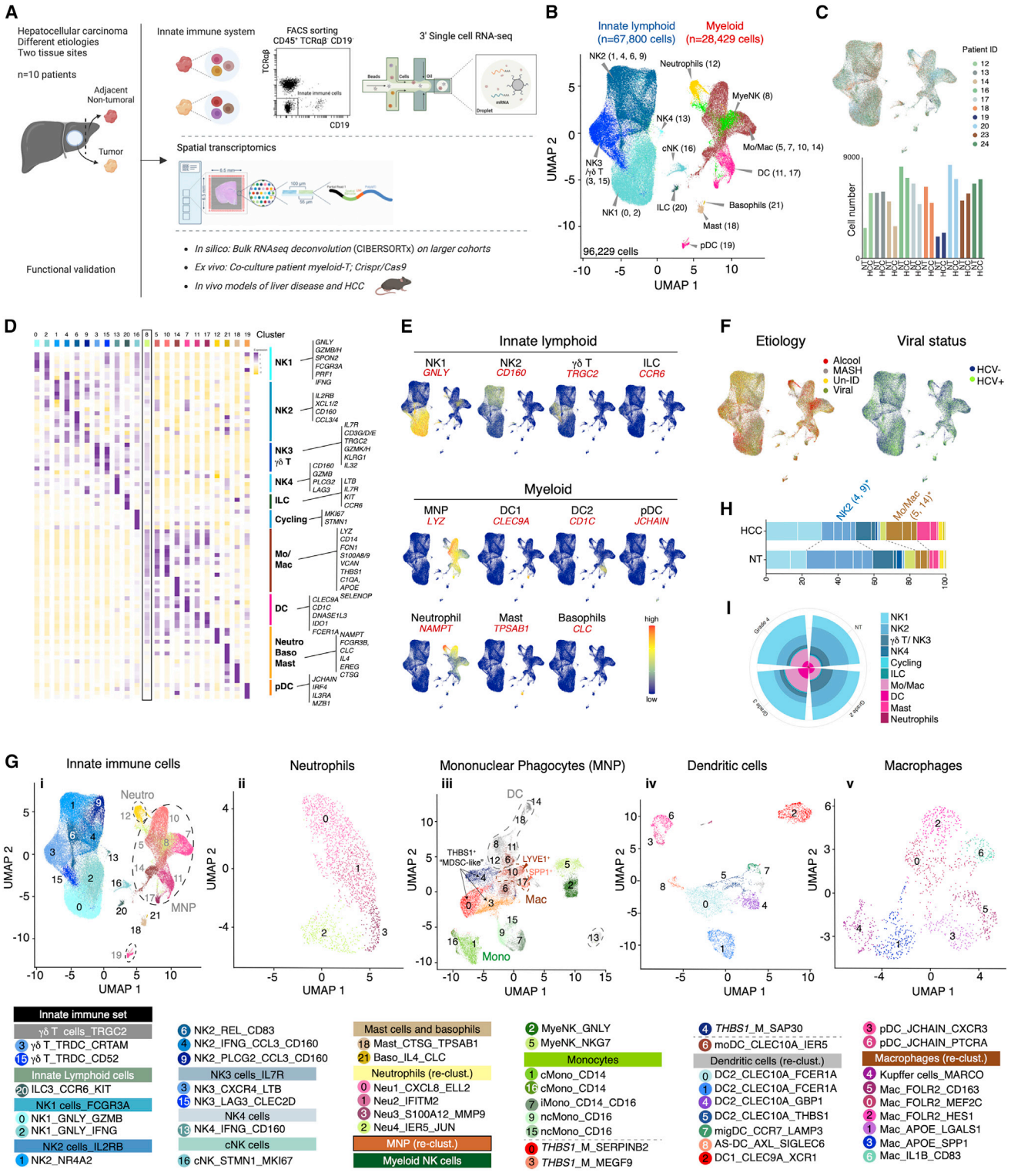

Figure 1. The innate immune landscape of hepatocellular carcinoma (HCC)

(A) Characterization of the hepatic innate immune cell landscape using scRNA-seq and stRNA-seq of tumors and adjacent NT tissue of 10 patients with hepatocellular carcinoma (HCC) of different etiologies.

(B) Louvain clustering of 96,229 scRNA-seq transcriptomes of innate immune cells in tumoral and NT tissues from 10 patients with HCC identifies 22 clusters.

(C) UMAP visualization and bar graph depicting cell numbers colored according to patient identity (ID).

(legend continued on next page)

mononuclear phagocytes (MNPs) and granulocytes, which exhibit remarkable heterogeneity according to ontogeny, inflammatory and metabolic signals, and tissue environments. The advent of single-cell and tracing technologies has unraveled the complexity of myeloid cell states, warranting context-specific characterization of deleterious subsets to direct targeted therapies.

While the cellular landscape of HCC has been previously described using single-cell approaches,[8–14] the impact of etiology on the diversity of the innate immune compartment, particularly myeloid cells, has not been fully characterized. Here, we implemented scRNA-seq on purified innate immune cells freshly isolated from tumoral and juxta-tumoral tissues from patients with HCC of different etiologies and performed spatial transcriptomics (stRNA-seq) to map their localization. We unravel a discrete thrombospondin (THBS)1$^+$ myeloid cell population, abundant in the tumor of patients with SLD-associated HCC that expresses monocyte- and neutrophil-affiliated genes and can be identified by co-expression of TREM1 and CD163. We refer to these cells as THBS1$^+$ regulatory myeloid (M_{reg}) cells, as they are potent suppressors of T cell activity *ex vivo*, a function further potentiated by TREM1 engagement, are spatially enriched at HCC fibrotic lesions, and co-occur with FAP$^+$ cancer-associated fibroblasts (CAFs) as revealed by stRNA-seq. Both THBS1$^+$ M_{reg} intra-tumoral density and *TREM1* median expression associate with high-grade HCC and poor prognosis. In experimental mouse models, specific inhibition of TREM1 signaling results in an immunogenic TME and rapid HCC tumor eradication. Our results elucidate THBS1$^+$ M_{reg} cells as a biomarker of severe HCC and a potential immunotherapeutic target.

RESULTS

The hepatic innate immune landscape in HCC

To characterize the innate immune landscape of HCC at high resolution, we implemented scRNA-seq (10x Genomics) on fluorescence-activated cell sorting (FACS)-enriched CD45$^+$ panTCR$\alpha\beta^-$CD19$^-$ cells freshly isolated from tumors (HCC) and adjacent non-tumoral (NT) liver sections. In parallel, we applied stRNA-seq (Visium, 10x Genomics) on frozen tissue sections from the same patients (Figure 1A). We included 10 HCC patients with different etiologies (HCV [n = 3], obesity [n = 5], excessive alcohol consumption [n = 3]) (Table S1). Steatohepatitis and fibrotic lesions were confirmed in liver NT and HCC sections by hematoxylin/eosin/saffron and trichrome staining (Figure S1A). For scRNA-seq, 15,000 innate immune viable cells were loaded on the 10x chip. Following putative doublet removal and exclusion of stressed or dead cells (Figure S1B; Table S2), we analyzed the transcriptomes of ~96,000 cells (~2,300 genes/cell) across 10 HCC (~46,000 cells) and 10 NT (~50,000 cells) samples. Following data processing, 22 Louvain clusters were identified (Figure 1B), containing cells from all patients and tissue sites (Figure 1C; Table S2). Using a scoring method based on signatures from Panglao DB, the expression of discriminatory features, and canonical markers (Figures 1D and 1E; Table S3), we identified the major innate immune cell populations (Figure 1B). At this initial resolution, we observed a lack of any specific population according to etiology or viral status (Figure 1F), consistent with previous studies.[9,10]

In total, we identified 11 innate lymphoid clusters (~68,000 cells), encompassing one innate lymphoid cell (ILC3) cluster (c20) and 10 clusters of natural killer (NK) cells (Figure 1G). These included one cycling NK cluster (c16; *STMN1*; *MKI67*), two NK1 clusters (c0, 2) representing *FCGR3A* (CD16)$^+$ cytotoxic NK cells (*FGFBP2*, *GNLY*, *CX3CR1*, *GZMB*, *PRF1*), and four liver-resident NK2 clusters (c1, 4, 6, 9) commonly expressing *IL2RB* and *CXCR6* but distinguished based on expression of inflammatory/anti-tumoral effectors (c4, 9; *IFNG*, *CCL3*, *CCL4L1*) versus tolerogenic factors (c1, 6; *NR4A2*).[15–18] Two mixed NK3/$\gamma\delta$ T clusters (c3, 15) and a smaller NK4 cluster (c13) were also unraveled (Figure 1G; Table S3).

For myeloid populations, our analysis revealed 10 clusters (~28,000 cells) including granulocytes, MNPs, and one cluster of NK cells (c8) expressing both lymphoid (*IL7R*, *GNLY*, *KLRF1*, *KLRD1*, *GZMH/K/B*, *IFNG*) and myeloid (*LYZ*, *HLA-DRA/B1*, *S100A8/9*, *SAT1*, *CST3*) genes (Figures 1D [box] and 1G; Table S3). Among the granulocytes, we identified mast cells (c18), a residual cluster of basophils (c21), and one subset of neutrophils, which formed a continuum of four states (Figure 1G). Neu1-3 expressed chemokines, matrix remodeling, and immunosuppressive factors (*CXCL8*, *CXCR4*, *MMP9*, *PTGS2*, *S100A12*, *PADI4*),[19] while Neu4 encompassed neutrophil-like monocytes (*IER5*, *JUN*).[20] While the frequency of neutrophils was not significantly different in HCC compared to NT in our dataset, specific myeloid subsets significantly infiltrated the tumor, whereas anti-tumoral NK2s (c4, 9) were excluded from the tumor core (Figures 1H and 1I; Table S2).

Identification of THBS1$^+$ myeloid cells distinct from monocytes, macrophages, and dendritic cells

To reliably identify and discriminate different MNP and granulocyte populations, we next established core signatures and validated their specificity by testing their performance in both the innate immune and MNP datasets. Macrophages, conventional dendritic cells (cDCs), and plasmacytoid DCs (pDCs) were well identified with our core signatures (Figures S1C and S1D), and their states were characterized by independent re-clustering

(D) Heatmap representing average expression of discriminating genes for each cluster.
(E) Feature plots representing the expression of innate immune cells canonical markers.
(F) UMAP visualization colored according to patient disease etiology or viral status.
(G) Louvain clusters colored based on cell type annotation of the global innate immune dataset and downstream re-clustering of populations marked by dotted lines. Neutrophils (ii) and MNPs (iii) were re-clustered from the initial innate immune set (i), while DCs (iv) and macrophages (v) were re-clustered from the MNP dataset (iii).
(H) Main cluster frequencies in HCC and NT tissue. *p < 0.05 using the multiple Wilcoxon test.
(I) Circular plot of major cell type frequencies in NT tissue and HCC of different tumor grades. See also Figure S1 and Tables S1, S2, and S3.

(Figures 1G and S1E). Among the MNPs, we identified two macrophage subsets, LYVE1$^+$ macrophages (c10), expressing lymphatic vessel endothelial hyaluronan receptor-1 (LYVE1), which marks tissue-resident peri-vascular macrophages, and SPP1$^+$ macrophages (c17), expressing Secreted Phospho-Protein 1 (SPP1, also known as osteopontin), which marks pro-tumoral macrophages[21] (Figure S1K; Table S3). Higher resolution clustering of their transcriptomes further distinguished seven macrophage subsets (Figures 1Gv and S1E, left), including one inflammatory (c6; *IL1B*, *CD83*, *CD86*), two FOLR2$^-$TREM2$^+$ (c1, 3), expressing in common *CD9*, *SPP1*, and *GPNMB* among others, and four FOLR2$^+$TREM2$^-$ (c0, c2, c4, c5). The latter included three tissue-resident macrophage (TRM)-like clusters[22] and one Kupffer cell (KC) cluster (c4; *MARCO*, *TIMD4*) expressing lower levels of *MRC1* (*CD206*). A previous study implicated NOTCH signaling in re-programming a subset of bone marrow (BM)-derived macrophages into FOLR2$^+$ TRM-like macrophages.[10] Cells in c2 expressed high levels of the NOTCH effector HES1 and scored highly for our TRM signature (Figure S1F; Table S3), suggesting that they might represent such a population. Among the TREM2$^+$SPP1$^+$ tumor-associated macrophages (TAMs) (Figure S1G), two subsets were distinguished based on differential expression of *CD163*, a *CD163*^{low} subset (TAM1 [c1]) with discriminatory expression of metallothioneins (*MT1X*, *MT1G*, *MT2A*), and a *CD163*^{high} subset (TAM3 [c3]) expressing higher levels of immune checkpoints, including *HAVCR2* (TIM3), *LGALS9* (galectin-9), *VSIR* (VISTA), *CD58*, and the metabolic immune checkpoint interleukin-4-induced-1 (*IL4I1*)[23] (Figure S1H).

DC re-clustering distinguished nine subsets including two subsets of pDCs (c3, 6; *JCHAIN*, *LILRA4*, *MZB1*, and *IL3RA*) and seven subsets of cDCs (Figures 1Giv and S1E right). DC1s (c2) were identified based on *CLEC9A*, *XCR1*, and *DNASE1L3* expression, and AS-DC (c8) expressed *AXL* and *SIGLEC6*, whereas migratory DCs (migDCs, c7),[24] also referred to as mature regulatory DCs (mregDCs),[25] expressed maturation and migration genes (*LAMP3*, *CCL19*, *CCR7*) (Figure S2C). While these subsets formed one cluster each, a notable heterogeneity was observed for DC2 forming four clusters that expressed in common *CD1C* and *CLEC10A* (Figure S2C). *FCER1A* marked DC2 c0 and c1, with c1 distinguished by high expression of *CD163*. c4 found in HCV-infected HCC patients exhibited a type I IFN signature (*IFITM3*, *GBP5*, *GBP1*, *VAMP5*), while c5 shared features with monocyte-derived DCs (moDCs), expressing monocyte-associated genes (*FCN1*, *S100A8/9*). migDC (c7) and DC2 (c4) were the only DC subsets significantly enriched in HCC compared to NT (Figure S1I).

Our analysis also distinguished different monocyte states. While all monocyte-related subsets (MNP c0, 1, 3, 4, 6, 7, 9, 15, 16) could be identified by selective expression of *FCN1* (Figure S1J), c1, 7, 9, 15, and 16 expressed the highest levels of *LILRB1* (Figure S1J), a marker of mature circulating monocytes.[26] These monocytes could be classified according to their *FCGR3A* (CD16) expression into CD14$^+$CD16$^-$ classical monocytes (cMonos) (c1, 16), CD14$^+$CD16$^+$ intermediate monocytes (iMonos) (c7), and CD14$^-$CD16$^+$ non-classical monocytes (ncMonos) (c9, 15) (Figure S1K). In contrast, three discrete clusters (c0, 3, 4) distinct from monocytes, macrophages, and DCs were identified based on selective expression of THBS1 (Figures S1J–S1M). These cells express both monocyte- (*FCN1*) and neutrophil- (*CSF3R*, *TREM1*, *CLEC4E*) affiliated genes (Figures S1J–S1L) and are enriched for signatures previously ascribed to myeloid-derived suppressor cells (MDSCs).[27]

Together, our data confirm the previously reported heterogeneity of myeloid cells in HCC[9,10,12] but unravel THBS1$^+$ M cells expressing MDSC-affiliated genes as distinct from monocytes, macrophages, DCs, and neutrophils.

Reclassification of MDSC states in HCC

Despite their significance in cancer progression, MDSCs are poorly annotated, and the phenotypic markers used to isolate them overlap with those of normal neutrophils and monocytes in both mice and humans.[28] Our analysis revealed three clusters of THBS1$^+$ M cells representing 27.4% of all MNPs analyzed. To better characterize them, we first elucidated a core signature of 10 genes (*THBS1*, *VCAN*, *S100A12*, *SERPINB2*, *SAP30*, *MEGF9*, *TREM1*, *VEGFA*, *OLR1*, *PHLDA1*) that identify them as c10 of the innate immune dataset (Figure 2A) and c0, 3, 4 of the MNP dataset (Figure S1D). Patients in TCGA_LIHC with higher mean expression of the THBS1$^+$ M core_signature have significantly poorer median overall survival (mOS) compared to patients with lower expression, independently of cancer stage, pathological features, or etiology (Figure 2B). *TREM1* encoding "triggering receptor expressed on myeloid cells 1" discriminated THBS1$^+$ M cells from all other MNPs (Figure 2C). The lectin-type oxidized low-density lipoprotein (LDL) receptor 1 (LOX-1, encoded by *OLR1*), previously described as a specific marker of human polymorphonuclear (PMN)-MDSC,[27] had the highest expression in c0 but was also detected in other monocytes at lower levels (Figure S2A), as in Travaglini et al.[29] In contrast, we identified *SERPINB2* that encodes the plasminogen activator inhibitor type 2 as a more robust marker of THBS1$^+$ M (c0) (Figure S2A). *MEGF9* (multiple EGF-like domains 9) was most highly expressed in THBS1$^+$ M (c3), while SAP30 (Sin3A-associated protein 30) discriminated THBS1$^+$ M (c4) (Figure S2A).

To elucidate the nature of the three THBS1$^+$ M subsets, we performed an analysis of differentially expressed genes (DEGs). This revealed that c0 top DEGs were neutrophil-affiliated genes, e.g., *CXCL8*, *NAMPT*, and *PLAUR* (Figure 2D; Table S4), and c3 was discriminated by monocyte lineage genes *ATF3*, *CD14*, *CSF3R*, *CACYBP*, *LGALS2*, and *LILRA5* (Figure 2E; Table S4), whereas c4 DEGs included genes affiliated to macrophages and DCs (*C1QA/B/C*, *CD163* and *CLEC10A*, *CST3*) in addition to genes shared with c0 and highly expressed in neutrophils (*NAMPT*, *OLR1*, *PHLDA1/2*, *PLAUR*) (Figures 2E and 2F; Table S4). To identify the possible origin of THBS1$^+$ M cells, we applied RNA velocity on the innate immune dataset, which revealed that the THBS1$^+$ M population does not originate from differentiated monocytes or neutrophils (Figure 2G) but from a moDC precursor, as shown by higher resolution velocity analysis of the MNP dataset (Figure 2H). To explore the dynamic regulation among the three THBS1$^+$ M subsets, we mapped their position along an inferred trajectory through Pseudotime ordering, which revealed three states (Figure 2I) with distinct temporally expressed genes along the Pseudotime (Figure S2B). Principal component analysis revealed that moDC (c6), migDC (c11),

CellPress
OPEN ACCESS

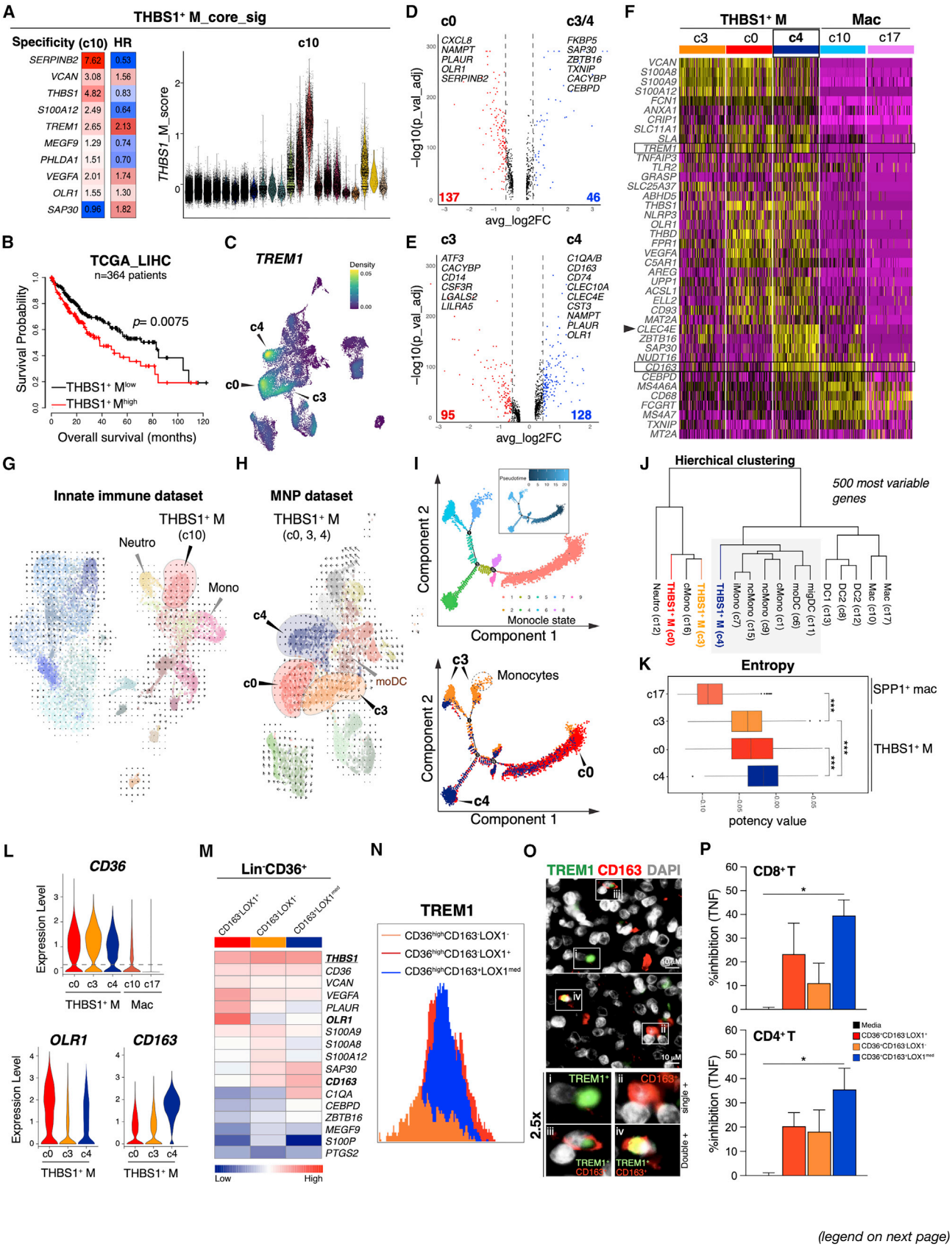

(legend on next page)

and THBS1$^+$ M (c4) occupied an intermediate transcriptional state between monocytes, macrophages, and DCs (Figure S2C). This was further confirmed by hierarchical clustering that connected THBS1$^+$ M (c4) to a branch containing moDC (c6) and migDC (c7) (Figure 2J). Calculation of differentiation potency estimates[31,32] revealed that THBS1$^+$ M (c4) had higher signaling promiscuity/entropy (higher capacity to differentiate to different lineages) compared to THBS1$^+$ M (c0), THBS1$^+$ M (c3), and SPP1$^+$ mac (c17) (Figure 2K). Similar results were obtained with predicted ordering of differentiation states by CYTOTRACE, which positioned THBS1$^+$ M (c4) in an intermediate state compared to DCs and monocytes/macrophages (Figure S2D).

We next sought to investigate the function of the three THBS1$^+$ M populations. We searched for cell surface proteins differentially expressed among them. We found that the scavenger receptor CD36 was highly expressed on all three THBS1$^+$ M subsets compared to macrophages (Figure 2L) or other MNPs (Figure S1K), and we identified *OLR1* (encoding LOX-1) and *CD163* as selective markers capable of distinguishing the three subsets apart (Figure 2L). This was validated by FACS (Figure S2E) and bulk RNA-seq of the sorted populations (Figures 2M–S2I; Table S4). Consistent with our scRNA-seq data (Figure 2C), *TREM1* was expressed on all three THBS1$^+$ M subsets albeit with higher surface expression on the CD36^{high}CD163$^-$LOX-1$^+$ (corresponding to c0) and CD36^{high}CD163$^+$LOX-1^{med} (corresponding to c4) populations (Figure 2N). Besides *TREM1*, THBS1$^+$ M (c4) selectively expressed *CLEC4E* (also primarily expressed on neutrophils) (Figures 2F and S1L). THBS1$^+$ M (c4) can thus be identified as CD36^{high}CD163$^+$LOX1^{med}TREM1^{high} CLEC4E$^+$, which we validated by immunofluorescence (IF) analysis of HCC patient tumors *in situ* using anti-CD163 with either anti-TREM1 or anti-CLEC4E (Figures 2O–S3C) and by FACS using a conventional "MDSC" staining strategy,[33] which further identified this CD163$^+$TREM1$^+$ population as CD33$^+$HLA-DR^{med} population (Figure S2F). To assess immunosuppressive activity, we co-cultured FACS-sorted myeloid subsets according to the strategy in Figure S2E with activated CD8$^+$ T or CD4$^+$ T cells purified from healthy donors or with a high-avidity Th1-polarized CD4$^+$ T cell clone reactive to telomerase (TERT) peptide UCP4, as in Lauret Marie Joseph et al.[34] All three subsets inhibited T cell production of effector cytokines (Figures 2P, S2G, and S2H), albeit the CD36$^+$CD163$^+$LOX-1^{med} population (corresponding to c4) showed the most potent inhibitory effect. As a control, we generated human monocyte-derived suppressor cells (HuMoSCs)[35] and confirmed that they suppressed cytokine production by activated T cells (Figures S2J and S2K). Phenotypic characterization of these HuMoSCs showed that they were primarily CD163$^+$ (>85%) and highly expressed TREM1 (Figures S2L and S2M), suggesting that an immunosuppressive capacity can be identified by dual expression of TREM1 and CD163. Myeloid cells exert their immunosuppressive functions through different mechanisms, e.g., via reactive oxygen species, nitric oxide, arginase, prostaglandin E2 (PGE_2), anti-inflammatory cytokines (e.g., IL-10 and TGFβ), and cell surface immune checkpoints such as PD-L1.[36] Interrogation of the expression of central effectors in these pathways revealed that THBS1$^+$ M (c4) expressed the highest levels of *TGFB1* (Figure S2N), which was also observed in *ex vivo*-generated HuMoSCs (Figure S2O). They also exhibited the highest levels of *IL13RA1*, which encodes a chain of the receptor for IL-13, a cytokine implicated in TGFβ induction.[37,38] In addition, they had elevated levels of *PTGES2* and *PTGER2*, encoding a PGE_2 synthase and receptor, respectively, as well as *ODC1*, encoding ornithine decarboxylase that acts downstream of arginase as the rate-limiting enzyme in the polyamine biosynthesis

Figure 2. Identification and characterization of THBS1$^+$ M_{reg} cells

(A) Left, THBS1$^+$ M (c10, innate immune dataset) core signature specificity and association with mOS in patients with HCC from TCGA_LIHC. HR, hazard ratio; right, violin plot depicting c10 signature score in innate immune clusters.

(B) Kaplan-Meier survival curves of patients with HCC (n = 364)[30] according to expression of the THBS1$^+$ M_core signature.

(C) Density plot representing the expression of TREM1 as a discriminatory marker of the three THBS1$^+$ M clusters of the MNP re-clustering.

(D) Volcano plot depicting DEGs between THBS1$^+$ M (c0) and other THBS1$^+$ M cells (c3+c4).

(E) Volcano plot depicting DEGs between THBS1$^+$ M (c3) and THBS1$^+$ M (c4).

(F) Heatmap representing the expression of selected genes from CIBERSORTx top 40 scored genes of THBS1$^+$ M (c4) signature. 100 cells in each cluster are shown.

(G) RNA velocity of innate immune cells.

(H) RNA velocity of MNPs.

(I) Pseudotime trajectory analysis using Monocle2 of the three THBS1$^+$ M clusters, colored by Monocle state (upper panel), Pseudotime (upper small panel), or Seurat cluster (lower panel).

(J) Phylogenetic relationships of MNPs and neutrophils based on the expression of top 500 most variable genes.

(K) Boxplots of signaling entropy rates (y axis, also named differentiation potency) in the three THBS1$^+$ M clusters and the SPP1$^+$ Mac cluster (c17). Center line, median; box limits, upper and lower quartiles; whiskers, maximum and minimum values. ***$p < 0.001$ using the Wilcoxon test.

(L) Violin plots depicting expression of *CD36*, *OLR1*, and *CD163* in the indicated MNP clusters.

(M) Expression of selected genes among the different FACS-sorted myeloid subsets (bulk transcriptomics data), normalized using the geometric mean expression of FACS-sorted innate immune cells from 6 HCC patients.

(N) Histograms depicting TREM1 expression among the different THBS1$^+$ M subsets according to differential expression of LOX-1 and CD163 in the Lin$^-$CD36^{high} population.

(O) Epifluorescence images of HCC tumor sections stained with antibodies against TREM1 (OPAL 520) and CD163 (OPAL 650) together with DAPI (gray) to label nuclei. Insets correspond to boxed regions.

(P) Quantification of the % inhibition of TNFα production by CD8$^+$ T and CD4$^+$ T cells stimulated with anti-CD3/CD28 beads in co-culture with different myeloid subsets sorted from HCC surgical resections according to the gating strategy in Figure S3E. n = 3 HCC patients. Error bars represent SEM. *$p < 0.05$ using the Kruskal-Wallis test. See also Figure S2 and Table S4.

CellPress
OPEN ACCESS

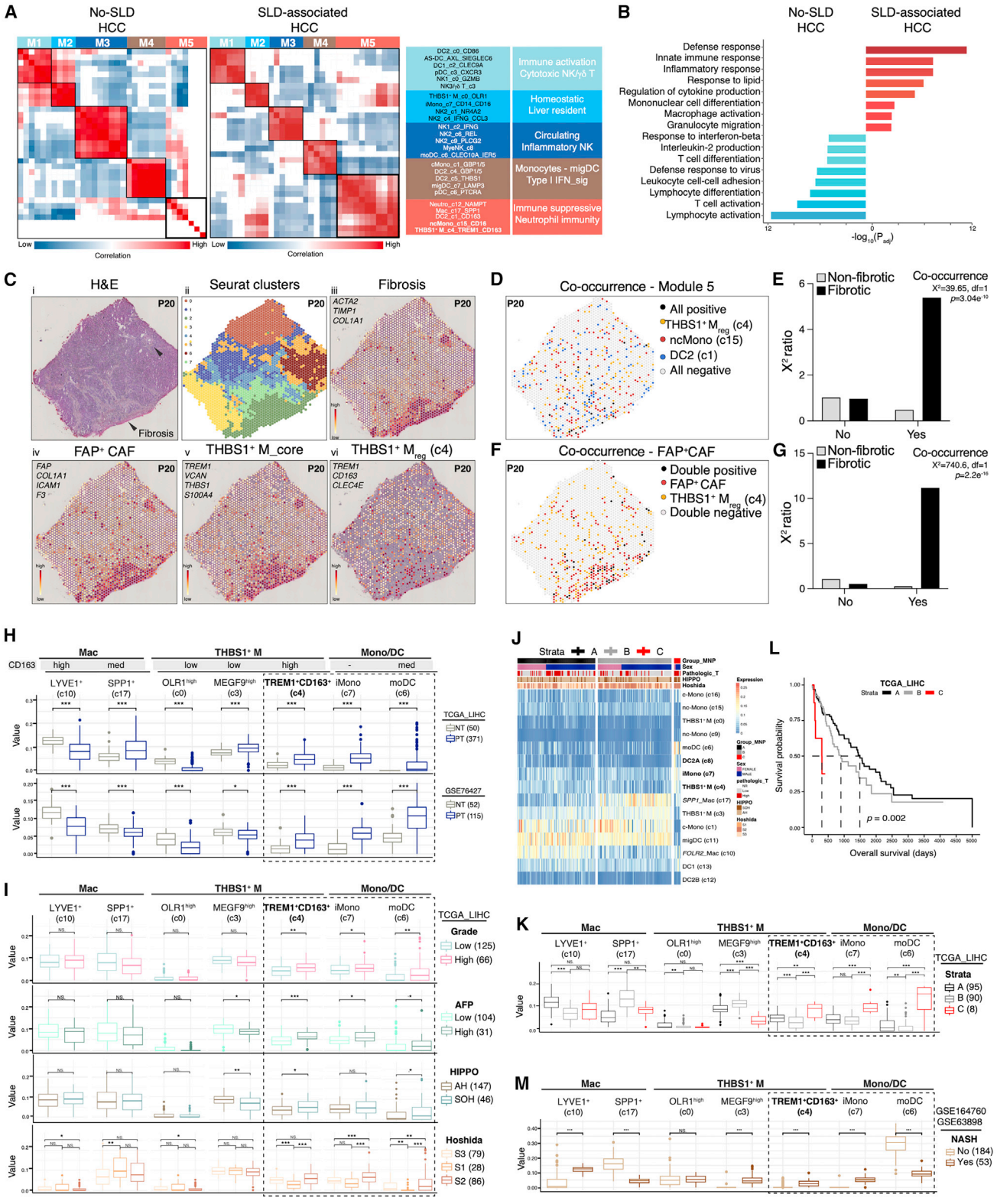

Figure 3. THBS1^{+} M$_{reg}$ cells expand in SLD-associated HCC and populate fibrotic lesions

(A) Cellular modules based on Pearson's correlations of cluster cell counts and further hierarchical clustering (SLD-associated HCC, n = 5; non-SLD HCC, n = 5). Non-significant correlations are represented by white squares ($p > 0.05$). Key clusters in each module are shown on the right. TIME, tumor immune microenvironment.

(legend continued on next page)

pathway. They shared with THBS1$^+$ M (c0) high expression of *ATF4*, encoding activating transcription factor 4, an endoplasmic reticulum stress effector required for MDSC immunosuppressive function.[39]

THBS1$^+$ M$_{reg}$ cells expand in SLD-associated HCC and are enriched at fibrotic lesions

To elucidate the impact of HCC etiology on the tumor immune microenvironment (TIME), we first defined innate immune cell subset co-occurrence by Pearson correlations among cluster counts from all patients (Figures 3A and S3A). This identified five cellular modules, including one (M5) enriched in neutrophil immunity and immunosuppressive pathways, encompassing THBS1$^+$ M$_{reg}$ (c4), which was significantly expanded in SLD-associated HCC in our discovery cohort (n = 10) (Figures 3A, 3B, S3A, and S3B; Table S4). To validate this observation, we quantified THBS1$^+$ M$_{reg}$ cells in tumor tissue sections from 10 additional HCC patients with or without SLD (n = 5 each) by IF staining with anti-CD163 and anti-CLEC4E antibodies. This analysis revealed increased CD163$^+$CLEC4E$^+$ cell numbers in SLD-compared to non-SLD-associated HCC (Figure S3C). To map the *in situ* distribution of these cells within tumors, we used stRNA-seq to analyze tissue sections from two patients with HCC containing fibrotic lesions. Transcriptomics from 2,261 to 1,987 spots were obtained at a median depth of 34,526 and 26,017 unique molecular identifiers (UMIs)/spot and 5,882 and 4,954 genes/spot for patients #20 and #23, respectively (Table S2). Unbiased clustering identified eight clusters in patient #20 (Figure 3C) and ten clusters in patient #23 (not shown). Based on spot feature expression, we identified clusters 2 and 5 in patient #20 and cluster 8 in patient #23 as scoring highly for a fibrosis signature (*COL1A1*, *TIMP1*, *ACTA2*) (Figures 3C and S3D). We next interrogated the *in situ* expression of a gene set (*TREM1*, *VCAN*, *THBS1*, *S100A4*) that discriminated THBS1$^+$ M cells from other innate immune cells (Figure S1M). Our results revealed an overlap in the expression of this gene set with that marking fibrotic lesions (Figures 3C and S3D). *VCAN*, *THBS1*, and *S100A4* may also be expressed by fibroblasts indicating that THBS1$^+$ M cells are geared with a pro-fibrotic machinery, consistent with their high expression of *TGFB1*, *IL13RA1* (Figure S2N), and *TIMP1* (Figure S1M). To ensure specific detection of THBS1$^+$ M (c4) cells, we next examined the expression of a more-restricted signature composed of *TREM1*, *CD163*, and *CLEC4E* (Figure S1K; Table S3). Our results revealed that THBS1$^+$ M (c4) cells were found at fibrotic lesions (Figures 3C and S3D). We next used linear regression and Pearson's chi-squared (X^2) to test the number of spots significantly enriched in multiple immune populations in both fibrotic and non-fibrotic regions of HCC. This analysis showed significant fibrosis-associated spatial cell-to-cell co-occurrence of THBS1$^+$ M$_{reg}$ (c4), ncMono (c15), and DC2 (c1), subsets enriched in the SLD-HCC-associated module M5 (Figures 3D, 3E, S3E, and S3F). Specific CAF sub-populations promote immunosuppression in the TME and have been linked to immunotherapy resistance.[40,41] Immunosuppressive CAFs exhibit an activated phenotype and express markers such as fibroblast-activation protein (*FAP*) and components of the desmoplastic structures, including collagens (*COL1A1*, *COL3A1*), integrins (*ICAM1*), and tissue factor (*F3*). We interrogated the spot feature expression of an FAP$^+$ CAF signature (*FAP*, *COL1A1*, *ICAM1*, *F3*) in our stRNA-seq data and observed overlapping spatial distribution with that of THBS1$^+$ M (c4) (Figures 3C and S3D), suggesting potential crosstalk between these two populations. This was further validated using spot co-occurrence (Figures 3F, 3G, S3G, and S3H) and cell-cell communication (CellChat) analyses uncovering significant pathways (Figure S3I) and cytokine ligand-receptor pairs (Figure S3J) predicted to mediate their functional interactions.

Together, these results point to a module of cells encompassing THBS1$^+$ M (c4) that expands in SLD-associated HCC and correlates with pro-fibrogenic, immunosuppressive CAFs in tumors.

(B) Pathway enrichment analysis using g:Profiler according to DEGs between SLD versus non-SLD in the innate immune dataset.
(C) Tumor section from a patient with HCC (P20) analyzed by stRNA-seq using Visium. i, tumor section stained with H&E; ii, overlapping localization of spatial Louvain Seurat clusters; spatial scoring of a gene signature marking (iii) fibrosis (*ACTA2*, *TIMP1*, *COL1A1*); (iv) FAP$^+$ CAFs (*FAP*, *COL1A1*, *ICAM1*, *F3*); (v) THBS1$^+$ M core (*TREM1*, *VCAN*, *THBS1*, *S100A4*); and (vi) THBS1$^+$ M$_{reg}$ (*TREM1*, *CD163*, *CLEC4E*).
(D) Spatial co-occurrence analysis of THBS1$^+$ M$_{reg}$ (c4), ncMono (c15), and DC2 (c1). Spots are colored according to absence of these populations (gray), presence of only one of them (yellow, red, or blue), or presence of the three populations (black).
(E) Chi-squared (X^2) statistics to test the co-occurrence of populations ("yes" for black spots or "no" for gray spots in D) in non-fibrotic (gray) or fibrotic (black) regions. X^2 ratio corresponds to observed/expected ratios (Roe).
(F) As in (D) but for spatial co-occurrence of THBS1$^+$ M$_{reg}$ (c4) and FAP$^+$ CAFs.
(G) As in (E).
(H) Boxplots depicting the predicted scores of macrophage, THBS1$^+$ M, and Mono/DC subsets by CIBERSORTx deconvolution of bulk transcriptomics data from two liver cancer cohorts (TCGA_LIHC and GSE76427). NT, non-tumoral; PT, primary tumor.
(I) Boxplots depicting the predicted scores of macrophage, THBS1$^+$ M, and Mono/DC subsets by CIBERSORTx deconvolution of bulk transcriptomics data from TCGA_LIHC according to tumor grade (low, pathologic T grade 1 and 2; high, pathologic T grade 3 and 4), serum AFP (<300 or >300), HIPPO status, or Hoshida class.
(J) Heatmap depicting predicted scores of MNP populations by CIBERSORTx deconvolution of bulk transcriptomics data from TCGA_LIHC. Unsupervised hierarchical clustering of patients depicts three strata: A, B, and C.
(K) Boxplots depicting the predicted scores of macrophage, THBS1$^+$ M, and Mono/DC subsets by CIBERSORTx deconvolution of bulk transcriptomics data from TCGA_LIHC according to strata identified in (J).
(L) Kaplan-Meier survival curves of patients with HCC (n = 193) from TCGA_LIHC stratified according to the three strata identified in (J) based on MNP infiltrate profiles.
(M) Boxplots depicting the predicted scores of macrophage, THBS1$^+$ M, and Mono/DC subsets by CIBERSORTx deconvolution of microarray expression data from patients with NASH-HCC or non-NASH-HCC (GSE164760 and GSE63898). Center line, median; box limits, upper and lower quartiles; whiskers, maximum and minimum values. ***p < 0.001, **p < 0.01, *p < 0.05 using Wilcoxon tests for (H), (I), (K), and (M). See also Figure S3 and Table S4.

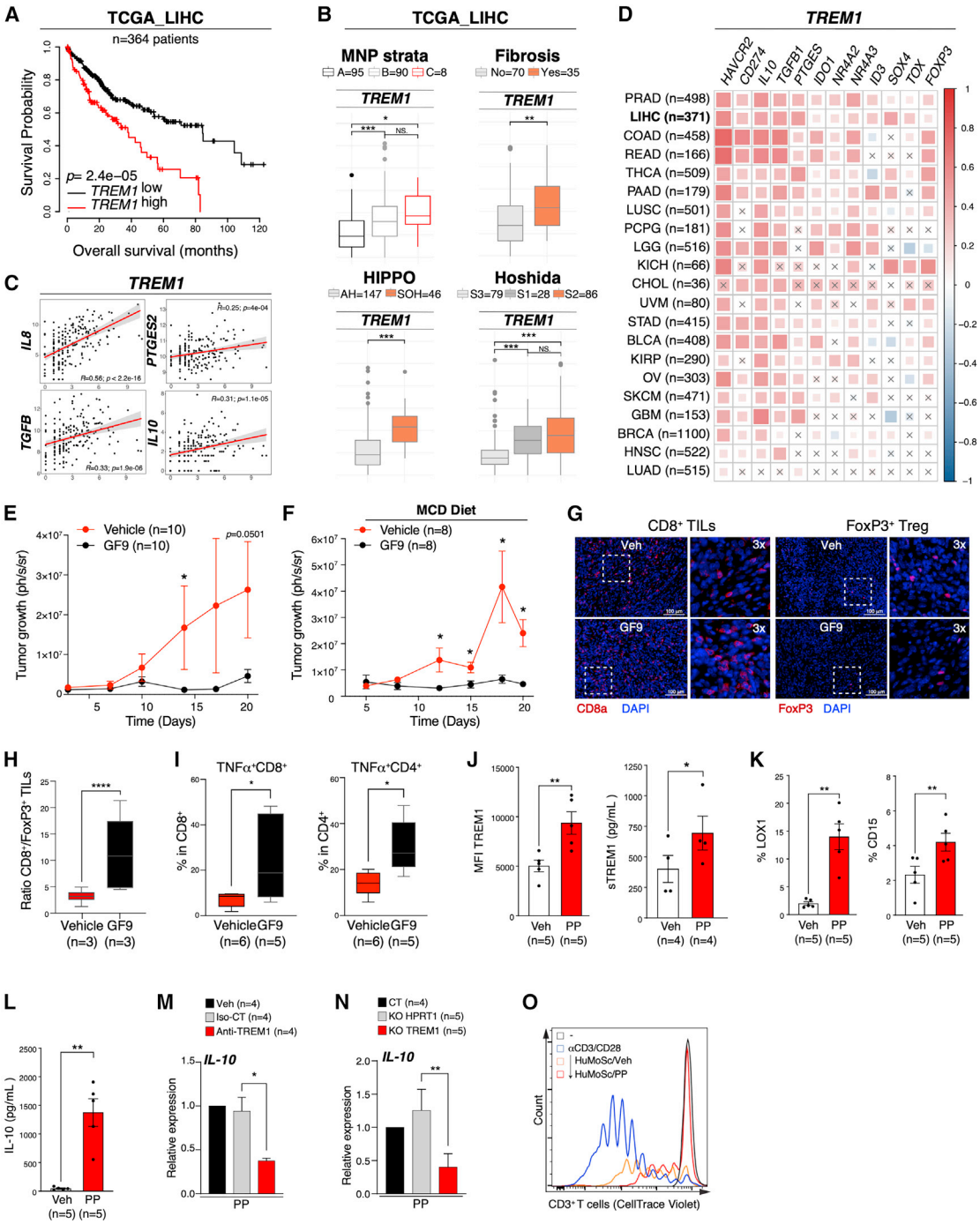

Figure 4. TREM1 associates with poor prognosis and contributes to the immunosuppressive activity of THBS1^{+} M_{reg} cells

(A) Kaplan-Meier survival curves of patients with HCC (n = 364)[30] according to *TREM1* expression.

(B) Boxplots depicting the expression of *TREM1* in TCGA_LIHC according to patient strata (Figure 3J), fibrosis, HIPPO status, or Hoshida class.

(C) Scatterplots depicting Pearson correlations between the log-normalized expression of *TREM1* and *TGFB*, *IL10*, *IL8*, or *PTGES2*.

(D) Correlation between the expression of *TREM1* and genes implicated in immunosuppression (*HAVCR2*, *CD274*, *IL10*, *TGFB1*, *PTGES*, *IDO1*), T cell exhaustion (*NR4A2/3*, *ID3*, *SOX4*, *TOX*), or T_{reg} (*FOXP3*) in different solid tumors. Values were obtained using TIMER2.0. Black crosses indicate non-significant correlations.

(E) Tumor volume by luminescence quantification in a transplantable liver orthotopic model of HCC using Hep55.1C cell line transduced with a lentivirus encoding luciferase. Mice were treated with a vehicle control or the TREM1 inhibitory peptide GF9. Pool of two independent experiments of 5 mice per condition. Error bars represent SEM. *p < 0.05 using the Mann-Whitney test.

(legend continued on next page)

THBS1$^+$ M_{reg} cells correlate with poor clinical outcomes in patients with HCC

To extend our findings to a larger cohorts of patients, we used the deconvolution algorithm CIBERSORTx[42] trained with our scRNA-seq data to infer the intra-tumoral abundance of MNP subsets defined in our study in primary tumors (PTs) and adjacent NT tissue of patients with HCC in two cohorts: TCGA_LIHC (371 patients) and GSE76427 (115 patients).[43] Our results show a consistent tumoral depletion of LYVE1$^+$ macrophages (c10) and OLR1^{high} PMN-MDSC-like (c0) in both cohorts but a variable distribution of SPP1$^+$ macrophages (c17) and MEGF9^{high} M-MDSC-like (c3) cells. In contrast, THBS1$^+$ M_{reg} (c4), iMono (c7), and moDC (c6) were consistently more abundant in the PT compared to NT tissue (Figures 3H and S3K) and associated with higher pathological tumor grade (stages III and IV), serum alpha-fetoprotein (AFP) levels, an important prognostic biomarker of mortality,[44] the silence of HIPPO [SOH] signature, reported to predict poor prognosis in patients with HCC,[45] and the Hoshida S2 subclass, characterized by larger and poorly differentiated tumors, elevated serum AFP, and poor mOS[46] (Figures 3I and S3L).

We wondered whether the nature of the myeloid infiltrate could stratify HCC patients and serve as an immunological biomarker of clinical outcomes. To address this, we performed unsupervised hierarchical clustering of HCC patients in TCGA_LIHC based on CIBERSORTx predicted scores of the MNP populations characterized in this study. Tumor-infiltrating MNP profiles divided HCC patients into three strata (Figures 3J and 3K) with significantly different mOS (Figure 3L). Group A patients with the best mOS had higher proportions of LYVE1$^+$ macrophages (c10) (Figures 3J–3l), whereas group B patients with an intermediate mOS had more SPP1$^+$ macrophages (c17) (Figures 3J–3l). Group C patients, with markedly reduced mOS (Figure 3L), had the highest proportions of THBS1$^+$ M_{reg} (c4), moDC (c6), and iMono (c7) (Figure 3K). Given the sexual dimorphism present in HCC patients, we further explored the effect of sex on estimated proportions of MNPs in TCGA_LIHC in each patient strata and quantified survival according to sex and MNP content. The data show sex-specific differences in MNP subsets and patient survival according to MNP class (Figures S3M and S3N). The analysis of sex-specific difference of the populations enriched in strata C (poorest survival) was limited by the small number of patients in this severe group. To extend our findings, we next examined the enrichment of THBS1$^+$ M_{reg} specifically in NASH-HCC. We explored two cohorts of patients (GSE164760 and GSE63898) including 53 with NASH-HCC and 184 with HCC of other etiologies. This analysis showed higher predicted content of THBS1$^+$ M_{reg} in patients with NASH-HCC (Figures 3M and S3O), identifying THBS1$^+$ M_{reg} cells, as a tumor-infiltrating myeloid cell population, enriched in SLD-HCC and associated with disease severity.

TREM1 confers immunosuppression and associates with poor prognosis in HCC

Among the 10 genes constituting the THBS1$^+$ M_core signature, *TREM1* confers the highest hazard ratio on HCC survival in TCGA_LIHC (Figures 2A and 4A), consistent with previous reports.[47,48] We wondered whether *TREM1* per se is associated with poor clinical outcomes and if it plays a direct role in immunosuppression. We interrogated *TREM1* expression in the three HCC patient groups from TCGA_LIHC classified according to MNP profiles. We observed the highest expression of *TREM1* in group C patients (Figure 4B), who have the highest content of THBS1$^+$ M_{reg} cells and the poorest mOS (Figures 3K–3L). In addition, *TREM1* was significantly associated with fibrosis, SOH status, and the Hoshida S2 class (Figure 4B). Expression of *TREM1* positively correlated with that of *TGFB*, *IL10*, *PTGES2*, and *IL8* in HCC (Figure 4C), as well as with several effectors of immunosuppression and CD8 T cell exhaustion in several solid tumors (Figure 4D), pointing to TREM1 as a potential effector of tumor progression and immunosuppression.

To experimentally address the role of TREM1 in HCC tumor control, we investigated the impact of its inhibition in mouse models, either in the absence or presence of underlying SLD, which was induced by feeding C57Bl/6 mice with a methionine- and choline-deficient (MCD) diet and evidenced by increased aspartate aminotransferase (AST) levels (Figure S4A) prior to Hep55.1C tumor orthotopic implantation. Our results show that

(F) C57BL6/J mice were fed a methionine- and choline-deficient (MCD) diet prior to tumor inoculation as in (E). n = 8 mice per condition. Error bars represent SEM. *p < 0.05 using the Mann-Whitney test.
(G) Epifluorescence images of Hep55.1C tumors liver sections from mice treated with vehicle control or GF9 as in (E) on day 20 post Hep55.1C injection stained with antibodies against CD8a or FoxP3 and DAPI to label nuclei. Insets correspond to boxed regions.
(H) Ratio of quantified stain-positive cells in (G). n = 3 mice per treatment. Error bars represent SEM. ****p < 0.0001 using the unpaired t test.
(I) Percentage (%) of TNF$^+$CD8$^+$ cells (left) and of TNF$^+$CD4$^+$ cells (right) in residual Hep55.1C tumors. n = 5 to 6 mice per condition. Error bars represent SEM. *p < 0.05 using the unpaired t test.
(J) Mean fluorescence intensity (MFI, median) of TREM1 expression on HuMoSC (left) and concentration of sTREM1 released from HuMoSC (right) treated on day 6 of differentiation with vehicle (water, white bars) or a complex of peptidoglycan (PGN) and PGN recognition protein 1 (PGLYRP1) (PP, red bars) for 24 h. n = 4–5 donors. Error bars represent SEM. *p < 0.05, **p < 0.01 using the paired t test.
(K) Quantification of HuMoSCs positive for the expression of LOX-1 or CD15 following a 24-h treatment with either vehicle (water) or PP as in (J). n = 5 donors. Error bars represent SEM. **p < 0.01 using the paired t test.
(L) Bar graphs depicting the concentration of soluble IL-10 released from HuMoSCs treated with vehicle (water) or PP as in (J). n = 5 donors. Error bars represent SEM. **p < 0.01 using the paired t test.
(M) Expression of *IL10* in HuMoSCs measured by qRT-PCR. HuMoSCs were treated with PP complex alone (vehicle, water) or together with ino-2 antibody that blocks TREM-1 (red bars) or isotype control (Iso-CT; gray bars). n = 4 donors. Error bars represent SEM. *p < 0.01 using the paired t test.
(N) Expression of *IL10* in HuMoSCs measured by qRT-PCR. HuMoSCs were treated with PP complex for 24 h. HuMoSCs were generated from monocytes nucleofected with sgHPRT1 (gray bars), sgTREM1 (red bars), or vehicle (PBS, black bars). n = 5 donors. Error bars represent SEM. **p < 0.01 using the paired t test.
(O) Representative FACS histogram depicting CellTrace Violet dilution as a readout of CD3$^+$ T cell proliferation over 6 days in the listed conditions. Veh, vehicle (water). See also Figure S4.

inhibition of TREM1 signaling by the GF9 peptide that interferes with TREM1 binding to its signaling adaptor DAP12[49] resulted in rapid tumor eradication (Figures 4E and 4F) and was more efficient than anti-PD-1 in the SLD context (Figure S4B). The effects of GF9 on tumor growth correlated with a significant increase in $CD8^+$/$FoxP3^+$ T cell ratio in the TME (Figures 4G and 4H) and enhanced T cell activation (Figure 4I). The rapid tumor eradication kinetics observed with GF9 was comparable to that with anti-Gr1 (Figure S4C), which depleted intra-tumoral $Ly6G^+$ $Ly6C^-$ cells expressing TREM1 (Figure S4D), arguing albeit indirectly that the observed GF9 effects are mediated by TREM1 inhibition on these cells. To address the specific role of TREM1 in myeloid cells, we used the HuMoSC model in co-culture with T cells *ex vivo*. We observed an induction of TREM1 cell surface expression in HuMoSC compared to monocytes (Figure S4E), suggesting that a suppressive function is linked to TREM1 expression. Treatment of HuMoSC with the TREM1 ligand PGLYRP1 (peptidoglycan recognition protein 1) in complex with peptidoglycan (PGN) (PP) further increased TREM1 cell surface expression and its release (sTREM1) (Figure 4J) and induced LOX-1 and CD15, two markers associated with a granulocytic phenotype (Figure 4K). In addition, PP induced IL-10 (Figure 4L), which was TREM1 dependent as demonstrated using anti-TREM1 antibody (Figure 4M) or *TREM1* knockout (Figures 4N and S4F). Importantly, TREM1 stimulation by PP further enhanced the capacity of HuMoSCs to suppress T cell proliferation (Figure 4O) and effector functions, e.g., inhibition of TNFα production (Figure S4G), which was partially mediated by IL-10 (Figure S4G). Together, these results suggest that the SLD environment promotes the expansion of $THBS1^+$ M_{reg} cells with strong immunosuppressive and pro-tumoral functions and point to TREM1 as a potential immunotherapeutic target in HCC.

DISCUSSION

Here, investigation of the innate immune cellular landscape of patients with HCC revealed previously unreported myeloid cell subsets. Our work presents four findings with important clinical implications: (1) HCC-associated genesis of cells with inter-myeloid mixed states, potentially stemming from emergency myelopoiesis[50] and/or trained immunity responses to tumor growth[51–53]; (2) a heterogeneity of myeloid states, yet with only specific subsets infiltrating the tumor; (3) identification of $THBS1^+$ M_{reg} subset with immunosuppressive activity that expands in the SLD setting, populates fibrotic lesions in HCC, and associates with poor prognosis; and (4) demonstration of a role of TREM1 in amplifying the immunosuppressive function of human monocyte-derived suppressor cells and in promoting HCC growth *in vivo*.

Our analysis demonstrates the heterogeneity of myeloid populations and shows that THBS1 expression marks myeloid cells enriched in MDSC signature.[27] They were found in three distinct states in HCC, including one with dual macrophage/DC and granulocyte features. Our results show that this subset exhibits a more potent immunosuppressive activity compared to other $THBS1^+$ M cells. We show, using spatial transcriptomics, that this subset populates fibrotic lesions in HCC in close association with pro-fibrogenic and pro-tumorigenic CAFs. This subset was more abundant in HCC in the SLD setting compared to other etiologies, as shown in our discovery and validation cohorts and predicted by deconvolution of larger patient cohort datasets.

TREM1 has been previously described as an amplifier of inflammation.[54] It was initially proposed to promote HCC development through pro-inflammatory cytokine production by Kupffer cells.[55] However, this early analysis used a non-discriminatory staining that marks a heterogeneous group of myeloid cells, preventing precise identification of deleterious myeloid cell subsets. Our scRNA-seq data reveal that TREM1 is a discriminatory feature of $THBS1^+$ M cells distinguishing them from other MNPs in the liver of HCC patients. We show that TREM1 expression per se is predictive of poor clinical outcomes in HCC and is associated with the expression of immunosuppression and exhaustion markers in several solid tumors. TREM1 has been implicated in mediating liver fibrosis[56] and immunotherapy resistance in a mouse model of liver cancer.[57] Additionally, a recent study[58] reported that sTREM1 might engage Robo2 to activate hepatic stellate cells and liver fibrosis, pointing to TREM1 as a deleterious molecule in liver diseases. We demonstrate that TREM1 ligation by cognate ligand on HuMoSCs promotes their acquisition of features linked to a suppressive phenotype and boosts their capacity to suppress T cell proliferation and effector functions.

Collectively, our study supports the stratification of patients according to HCC etiology to define optimal therapeutic regimens, and it points to TREM1 targeting as an attractive therapeutic option in SLD-associated HCC.

Limitations of the study

In this study, we characterized the innate immune landscape of a small cohort of patients with HCC and identified a subset of $THBS1^+$ myeloid cells that expands in the SLD etiology. Future studies are needed to identify this population by multiplex immunofluorescence in larger patient cohorts. These studies will also help to interrogate the emergence of this myeloid population by SLD triggers and its functional relationship with other cells in the TME. Specific deletion of *Trem1* in the myeloid compartment and application of additional models of SLD will help determine the extent to which the observed effects of GF9 are attributed to TREM1 expression on myeloid cells with features similar to $THBS1^+$ M_{reg} cells.

STAR★METHODS

Detailed methods are provided in the online version of this paper and include the following:

- KEY RESOURCES TABLE
- RESOURCE AVAILABILITY
  - Lead contact
  - Materials availability
  - Data and code availability
- EXPERIMENTAL MODEL AND STUDY PARTICIPANT DETAILS
  - Study participants
  - Animal models
  - Cell culture

- METHOD DETAILS
  - Generation of HuMoSCs
  - CRISPR/Cas9 mediated TREM1 Knock-out
  - Human tissue dissociation
  - Flow cytometry staining
  - Single-cell FACS sorting
  - scRNA-seq
  - Visium spatial gene expression processing
  - Co-culture experiments
  - MCD-diet mouse model
  - Orthotopic tumor injection and tumor growth monitoring
  - Mouse tumor dissociation
  - Immunofluorescence and multiplex Immunohistochemistry staining and imaging
  - RNA extraction and RT-qPCR
  - Transcriptomic analyses of sorted innate immune cells and sorted THBS1^{+} myeloid cells – Sample preparation
  - scRNA-seq data processing, quality control and cleaning
  - Cell doublet detection and removal
  - Normalization and data integration
  - Unsupervised clustering, dimensionality reduction and data visualization
  - Cell type/state annotation
  - Identification of signature genes
  - Phylogenetic relationships of clusters based on gene expression
  - Trajectory inference
  - RNA velocity estimation
  - Estimation of differentiation potency or signaling entropy
  - Differential expression analysis, gene ontology and gene set enrichment analysis
  - Pre-processing and visualization of spatial transcriptomic data
  - Spatial co-occurrence analysis
  - Cell-cell communication analysis
  - Transcriptomic source data of external cohorts
  - Immuno-deconvolution and cancer genomics
  - Transcriptomic analyses of sorted innate immune cells and sorted THBS1+ monocytes – data processing and analysis
- QUANTIFICATION AND STATISTICAL ANALYSIS

SUPPLEMENTAL INFORMATION

Supplemental information can be found online at https://doi.org/10.1016/j.celrep.2024.113773.

ACKNOWLEDGMENTS

We thank Aurélia Le Dantec, Gaël Galli, and Sébastian Lillo from the Saleh lab for help and advice and Marie-Elise Truchetet, Damien Brisou, Elodie Sifré, and Christine Varon from the University of Bordeaux for materials and technical support. We thank Alexander B. Sigalov (SignaBlok, Inc.) for advice on GF9 peptide utilization *in vivo* and the Llovet team for help on best annotating NASH and non-NASH cohorts. We thank TBMCore platforms (CBiB, CRISP'edit, FACSility, One Cell, and Histopatology platforms), the Magendie Neurocenter laser microdissection platform, the Bordeaux Imaging Center, the GeT-Santé facility in Toulouse, and the CRB-K (Center de Ressources Biologiques – Cancer) of Bordeaux University Hospital. This work is funded by operating grants to M.S. from the ARC foundation, IDEX Bordeaux, and ITMO cancer and an infrastructure grant to M.S. from the New Aquitaine region. J.G. and D.C. are funded by the ARC foundation and ITMO cancer, and E.R. received a studentship from the SIRIC BRIO. J.G., D.C., and E.R. also received salary support from the New Aquitaine region.

AUTHOR CONTRIBUTIONS

Conceptualization, J.G., D.C., and M.S.; investigation, J.G., D.C., E.R., T.B., A.Z., and M.-A.D.; formal analysis, J.G., D.C., and M.S.; resources, N.L., O.A., B.L., C.L., L.C., and M.D.; writing—original draft, M.S.; writing—review & editing, J.G, D.C., and M.S.; supervision, M.N. and M.S.; funding acquisition, M.S. All of the authors commented on the manuscript.

DECLARATION OF INTERESTS

M.D. is co-founder, chief scientific officer, and employee of Inotrem SA, a French company that develops TREM1 inhibitors.

Received: April 19, 2023
Revised: November 5, 2023
Accepted: January 25, 2024
Published: February 12, 2024

REFERENCES

1. Rinella, M.E., Lazarus, J.V., Ratziu, V., Francque, S.M., Sanyal, A.J., Kanwal, F., Romero, D., Abdelmalek, M.F., Anstee, Q.M., Arab, J.P., et al. (2023). A multisociety Delphi consensus statement on new fatty liver disease nomenclature. Hepatology *78*, 1966–1986. https://doi.org/10.1097/HEP.0000000000000520.
2. Llovet, J.M., Kelley, R.K., Villanueva, A., Singal, A.G., Pikarsky, E., Roayaie, S., Lencioni, R., Koike, K., Zucman-Rossi, J., and Finn, R.S. (2021). Hepatocellular carcinoma. Nat. Rev. Dis. Primers *7*, 6. https://doi.org/10.1038/s41572-020-00240-3.
3. Finn, R.S., Qin, S., Ikeda, M., Galle, P.R., Ducreux, M., Kim, T.Y., Kudo, M., Breder, V., Merle, P., Kaseb, A.O., et al. (2020). Atezolizumab plus Bevacizumab in Unresectable Hepatocellular Carcinoma. N. Engl. J. Med. *382*, 1894–1905. https://doi.org/10.1056/NEJMoa1915745.
4. Abou-Alfa, G.K., Lau, G., Kudo, M., Chan, S.L., Kelley, R.K., Furuse, J., Sukeepaisarnjaroen, W., Kang, Y.K., Van Dao, T., De Toni, E.N., et al. (2022). Tremelimumab plus Durvalumab in Unresectable Hepatocellular Carcinoma. NEJM Evid. *1*. https://doi.org/10.1056/EVIDoa2100070.
5. Giraud, J., Chalopin, D., Blanc, J.F., and Saleh, M. (2021). Hepatocellular Carcinoma Immune Landscape and the Potential of Immunotherapies. Front. Immunol. *12*, 655697. https://doi.org/10.3389/fimmu.2021.655697.
6. Pfister, D., Núñez, N.G., Pinyol, R., Govaere, O., Pinter, M., Szydlowska, M., Gupta, R., Qiu, M., Deczkowska, A., Weiner, A., et al. (2021). NASH limits anti-tumour surveillance in immunotherapy-treated HCC. Nature *592*, 450–456. https://doi.org/10.1038/s41586-021-03362-0.
7. Goswami, S., Anandhan, S., Raychaudhuri, D., and Sharma, P. (2023). Myeloid cell-targeted therapies for solid tumours. Nat. Rev. Immunol. *23*, 106–120. https://doi.org/10.1038/s41577-022-00737-w.
8. Zheng, C., Zheng, L., Yoo, J.K., Guo, H., Zhang, Y., Guo, X., Kang, B., Hu, R., Huang, J.Y., Zhang, Q., et al. (2017). Landscape of Infiltrating T Cells in Liver Cancer Revealed by Single-Cell Sequencing. Cell *169*, 1342–1356.e16. https://doi.org/10.1016/j.cell.2017.05.035.
9. Zhang, Q., He, Y., Luo, N., Patel, S.J., Han, Y., Gao, R., Modak, M., Carotta, S., Haslinger, C., Kind, D., et al. (2019). Landscape and Dynamics of Single Immune Cells in Hepatocellular Carcinoma. Cell *179*, 829–845.e20. https://doi.org/10.1016/j.cell.2019.10.003.
10. Sharma, A., Seow, J.J.W., Dutertre, C.A., Pai, R., Blériot, C., Mishra, A., Wong, R.M.M., Singh, G.S.N., Sudhagar, S., Khalilnezhad, S., et al.

(2020). Onco-fetal Reprogramming of Endothelial Cells Drives Immunosuppressive Macrophages in Hepatocellular Carcinoma. Cell *183*, 377–394.e21. https://doi.org/10.1016/j.cell.2020.08.040.

11. Song, G., Shi, Y., Zhang, M., Goswami, S., Afridi, S., Meng, L., Ma, J., Chen, Y., Lin, Y., Zhang, J., et al. (2020). Global immune characterization of HBV/HCV-related hepatocellular carcinoma identifies macrophage and T-cell subsets associated with disease progression. Cell Discov. *6*, 90. https://doi.org/10.1038/s41421-020-00214-5.
12. Sun, Y., Wu, L., Zhong, Y., Zhou, K., Hou, Y., Wang, Z., Zhang, Z., Xie, J., Wang, C., Chen, D., et al. (2021). Single-cell landscape of the ecosystem in early-relapse hepatocellular carcinoma. Cell *184*, 404–421.e16. https://doi.org/10.1016/j.cell.2020.11.041.
13. Ma, L., Hernandez, M.O., Zhao, Y., Mehta, M., Tran, B., Kelly, M., Rae, Z., Hernandez, J.M., Davis, J.L., Martin, S.P., et al. (2019). Tumor Cell Biodiversity Drives Microenvironmental Reprogramming in Liver Cancer. Cancer Cell *36*, 418–430.e6. https://doi.org/10.1016/j.ccell.2019.08.007.
14. Ma, L., Wang, L., Khatib, S.A., Chang, C.W., Heinrich, S., Dominguez, D.A., Forgues, M., Candia, J., Hernandez, M.O., Kelly, M., et al. (2021). Single-cell atlas of tumor cell evolution in response to therapy in hepatocellular carcinoma and intrahepatic cholangiocarcinoma. J. Hepatol. *75*, 1397–1408. https://doi.org/10.1016/j.jhep.2021.06.028.
15. Hibino, S., Chikuma, S., Kondo, T., Ito, M., Nakatsukasa, H., Omata-Mise, S., and Yoshimura, A. (2018). Inhibition of Nr4a Receptors Enhances Antitumor Immunity by Breaking Treg-Mediated Immune Tolerance. Cancer Res. *78*, 3027–3040. https://doi.org/10.1158/0008-5472.CAN-17-3102.
16. Sekiya, T., Kashiwagi, I., Inoue, N., Morita, R., Hori, S., Waldmann, H., Rudensky, A.Y., Ichinose, H., Metzger, D., Chambon, P., and Yoshimura, A. (2011). The nuclear orphan receptor Nr4a2 induces Foxp3 and regulates differentiation of CD4+ T cells. Nat. Commun. *2*, 269. https://doi.org/10.1038/ncomms1272.
17. Liu, X., Wang, Y., Lu, H., Li, J., Yan, X., Xiao, M., Hao, J., Alekseev, A., Khong, H., Chen, T., et al. (2019). Genome-wide analysis identifies NR4A1 as a key mediator of T cell dysfunction. Nature *567*, 525–529. https://doi.org/10.1038/s41586-019-0979-8.
18. Seo, H., Chen, J., González-Avalos, E., Samaniego-Castruita, D., Das, A., Wang, Y.H., López-Moyado, I.F., Georges, R.O., Zhang, W., Onodera, A., et al. (2019). TOX and TOX2 transcription factors cooperate with NR4A transcription factors to impose CD8(+) T cell exhaustion. Proc. Natl. Acad. Sci. USA *116*, 12410–12415. https://doi.org/10.1073/pnas.1905675116.
19. Zhu, Y.P., Eggert, T., Araujo, D.J., Vijayanand, P., Ottensmeier, C.H., and Hedrick, C.C. (2020). CyTOF mass cytometry reveals phenotypically distinct human blood neutrophil populations differentially correlated with melanoma stage. J. Immunother. Cancer *8*, e000473. https://doi.org/10.1136/jitc-2019-000473.
20. Yáñez, A., Coetzee, S.G., Olsson, A., Muench, D.E., Berman, B.P., Hazelett, D.J., Salomonis, N., Grimes, H.L., and Goodridge, H.S. (2017). Granulocyte-Monocyte Progenitors and Monocyte-Dendritic Cell Progenitors Independently Produce Functionally Distinct Monocytes. Immunity *47*, 890–902.e4. https://doi.org/10.1016/j.immuni.2017.10.021.
21. Bill, R., Wirapati, P., Messemaker, M., Roh, W., Zitti, B., Duval, F., Kiss, M., Park, J.C., Saal, T.M., Hoelzl, J., et al. (2023). CXCL9:SPP1 macrophage polarity identifies a network of cellular programs that control human cancers. Science *381*, 515–524. https://doi.org/10.1126/science.ade2292.
22. Nalio Ramos, R., Missolo-Koussou, Y., Gerber-Ferder, Y., Bromley, C.P., Bugatti, M., Núñez, N.G., Tosello Boari, J., Richer, W., Menger, L., Denizeau, J., et al. (2022). Tissue-resident FOLR2(+) macrophages associate with CD8(+) T cell infiltration in human breast cancer. Cell *185*, 1189–1207.e25. https://doi.org/10.1016/j.cell.2022.02.021.
23. Sadik, A., Somarribas Patterson, L.F., Öztürk, S., Mohapatra, S.R., Panitz, V., Secker, P.F., Pfänder, P., Loth, S., Salem, H., Prentzell, M.T., et al. (2020). IL4I1 Is a Metabolic Immune Checkpoint that Activates the AHR and Promotes Tumor Progression. Cell *182*, 1252–1270.e34. https://doi.org/10.1016/j.cell.2020.07.038.
24. Miller, J.C., Brown, B.D., Shay, T., Gautier, E.L., Jojic, V., Cohain, A., Pandey, G., Leboeuf, M., Elpek, K.G., Helft, J., et al. (2012). Deciphering the transcriptional network of the dendritic cell lineage. Nat. Immunol. *13*, 888–899. https://doi.org/10.1038/ni.2370.
25. Maier, B., Leader, A.M., Chen, S.T., Tung, N., Chang, C., LeBerichel, J., Chudnovskiy, A., Maskey, S., Walker, L., Finnigan, J.P., et al. (2020). A conserved dendritic-cell regulatory program limits antitumour immunity. Nature *580*, 257–262. https://doi.org/10.1038/s41586-020-2134-y.
26. Weinreb, C., Rodriguez-Fraticelli, A., Camargo, F.D., and Klein, A.M. (2020). Lineage tracing on transcriptional landscapes links state to fate during differentiation. Science *367*, eaaw3381. https://doi.org/10.1126/science.aaw3381.
27. Condamine, T., Dominguez, G.A., Youn, J.I., Kossenkov, A.V., Mony, S., Alicea-Torres, K., Tcyganov, E., Hashimoto, A., Nefedova, Y., Lin, C., et al. (2016). Lectin-type oxidized LDL receptor-1 distinguishes population of human polymorphonuclear myeloid-derived suppressor cells in cancer patients. Sci. Immunol. *1*, aaf8943. https://doi.org/10.1126/sciimmunol.aaf8943.
28. Veglia, F., Sanseviero, E., and Gabrilovich, D.I. (2021). Myeloid-derived suppressor cells in the era of increasing myeloid cell diversity. Nat. Rev. Immunol. *21*, 485–498. https://doi.org/10.1038/s41577-020-00490-y.
29. Travaglini, K.J., Nabhan, A.N., Penland, L., Sinha, R., Gillich, A., Sit, R.V., Chang, S., Conley, S.D., Mori, Y., Seita, J., et al. (2020). A molecular cell atlas of the human lung from single-cell RNA sequencing. Nature *587*, 619–625. https://doi.org/10.1038/s41586-020-2922-4.
30. Menyhárt, O., Nagy, Á., and Győrffy, B. (2018). Determining consistent prognostic biomarkers of overall survival and vascular invasion in hepatocellular carcinoma. R. Soc. Open Sci. *5*, 181006. https://doi.org/10.1098/rsos.181006.
31. Teschendorff, A.E., and Enver, T. (2017). Single-cell entropy for accurate estimation of differentiation potency from a cell's transcriptome. Nat. Commun. *8*, 15599. https://doi.org/10.1038/ncomms15599.
32. Teschendorff, A.E., Maity, A.K., Hu, X., Weiyan, C., and Lechner, M. (2021). Ultra-fast scalable estimation of single-cell differentiation potency from scRNA-Seq data. Bioinformatics *37*, 1528–1534. https://doi.org/10.1093/bioinformatics/btaa987.
33. Bronte, V., Brandau, S., Chen, S.H., Colombo, M.P., Frey, A.B., Greten, T.F., Mandruzzato, S., Murray, P.J., Ochoa, A., Ostrand-Rosenberg, S., et al. (2016). Recommendations for myeloid-derived suppressor cell nomenclature and characterization standards. Nat. Commun. *7*, 12150. https://doi.org/10.1038/ncomms12150.
34. Lauret Marie Joseph, E., Laheurte, C., Jary, M., Boullerot, L., Asgarov, K., Gravelin, E., Bouard, A., Rangan, L., Dosset, M., Borg, C., and Adotévi, O. (2020). Immunoregulation and Clinical Implications of ANGPT2/TIE2(+) M-MDSC Signature in Non-Small Cell Lung Cancer. Cancer Immunol. Res. *8*, 268–279. https://doi.org/10.1158/2326-6066.CIR-19-0326.
35. Janikashvili, N., Trad, M., Gautheron, A., Samson, M., Lamarthée, B., Bonnefoy, F., Lemaire-Ewing, S., Ciudad, M., Rekhviashvili, K., Seaphanh, F., et al. (2015). Human monocyte-derived suppressor cells control graft-versus-host disease by inducing regulatory forkhead box protein 3-positive CD8+ T lymphocytes. J. Allergy Clin. Immunol. *135*, 1614–1624.e4. https://doi.org/10.1016/j.jaci.2014.12.1868.
36. Hegde, S., Leader, A.M., and Merad, M. (2021). MDSC: Markers, development, states, and unaddressed complexity. Immunity *54*, 875–884. https://doi.org/10.1016/j.immuni.2021.04.004.
37. Fichtner-Feigl, S., Strober, W., Kawakami, K., Puri, R.K., and Kitani, A. (2006). IL-13 signaling through the IL-13alpha2 receptor is involved in induction of TGF-beta1 production and fibrosis. Nat. Med. *12*, 99–106. https://doi.org/10.1038/nm1332.
38. Lee, C.G., Homer, R.J., Zhu, Z., Lanone, S., Wang, X., Koteliansky, V., Shipley, J.M., Gotwals, P., Noble, P., Chen, Q., et al. (2001). Interleukin-13 induces tissue fibrosis by selectively stimulating and activating transforming growth factor beta(1). J. Exp. Med. *194*, 809–821. https://doi.org/10.1084/jem.194.6.809.

39. Halaby, M.J., Hezaveh, K., Lamorte, S., Ciudad, M.T., Kloetgen, A., MacLeod, B.L., Guo, M., Chakravarthy, A., Medina, T.D.S., Ugel, S., et al. (2019). GCN2 drives macrophage and MDSC function and immunosuppression in the tumor microenvironment. Sci. Immunol. *4*, eaax8189. https://doi.org/10.1126/sciimmunol.aax8189.

40. Kieffer, Y., Hocine, H.R., Gentric, G., Pelon, F., Bernard, C., Bourachot, B., Lameiras, S., Albergante, L., Bonneau, C., Guyard, A., et al. (2020). Single-Cell Analysis Reveals Fibroblast Clusters Linked to Immunotherapy Resistance in Cancer. Cancer Discov. *10*, 1330–1351. https://doi.org/10.1158/2159-8290.CD-19-1384.

41. Qi, J., Sun, H., Zhang, Y., Wang, Z., Xun, Z., Li, Z., Ding, X., Bao, R., Hong, L., Jia, W., et al. (2022). Single-cell and spatial analysis reveal interaction of FAP(+) fibroblasts and SPP1(+) macrophages in colorectal cancer. Nat. Commun. *13*, 1742. https://doi.org/10.1038/s41467-022-29366-6.

42. Steen, C.B., Liu, C.L., Alizadeh, A.A., and Newman, A.M. (2020). Profiling Cell Type Abundance and Expression in Bulk Tissues with CIBERSORTx. Methods Mol. Biol. *2117*, 135–157. https://doi.org/10.1007/978-1-0716-0301-7_7.

43. Grinchuk, O.V., Yenamandra, S.P., Iyer, R., Singh, M., Lee, H.K., Lim, K.H., Chow, P.K.H., and Kuznetsov, V.A. (2018). Tumor-adjacent tissue co-expression profile analysis reveals pro-oncogenic ribosomal gene signature for prognosis of resectable hepatocellular carcinoma. Mol. Oncol. *12*, 89–113. https://doi.org/10.1002/1878-0261.12153.

44. Tsukuma, H., Hiyama, T., Tanaka, S., Nakao, M., Yabuuchi, T., Kitamura, T., Nakanishi, K., Fujimoto, I., Inoue, A., Yamazaki, H., et al. (1993). Risk factors for hepatocellular carcinoma among patients with chronic liver disease. N. Engl. J. Med. *328*, 1797–1801. https://doi.org/10.1056/NEJM199306243282501.

45. Sohn, B.H., Shim, J.J., Kim, S.B., Jang, K.Y., Kim, S.M., Kim, J.H., Hwang, J.E., Jang, H.J., Lee, H.S., Kim, S.C., et al. (2016). Inactivation of Hippo Pathway Is Significantly Associated with Poor Prognosis in Hepatocellular Carcinoma. Clin. Cancer Res. *22*, 1256–1264. https://doi.org/10.1158/1078-0432.CCR-15-1447.

46. Hoshida, Y., Nijman, S.M.B., Kobayashi, M., Chan, J.A., Brunet, J.P., Chiang, D.Y., Villanueva, A., Newell, P., Ikeda, K., Hashimoto, M., et al. (2009). Integrative transcriptome analysis reveals common molecular subclasses of human hepatocellular carcinoma. Cancer Res. *69*, 7385–7392. https://doi.org/10.1158/0008-5472.CAN-09-1089.

47. Liao, R., Sun, T.W., Yi, Y., Wu, H., Li, Y.W., Wang, J.X., Zhou, J., Shi, Y.H., Cheng, Y.F., Qiu, S.J., and Fan, J. (2012). Expression of TREM-1 in hepatic stellate cells and prognostic value in hepatitis B-related hepatocellular carcinoma. Cancer Sci. *103*, 984–992. https://doi.org/10.1111/j.1349-7006.2012.02273.x.

48. Duan, M., Wang, Z.C., Wang, X.Y., Shi, J.Y., Yang, L.X., Ding, Z.B., Gao, Q., Zhou, J., and Fan, J. (2015). TREM-1, an inflammatory modulator, is expressed in hepatocellular carcinoma cells and significantly promotes tumor progression. Ann. Surg Oncol. *22*, 3121–3129. https://doi.org/10.1245/s10434-014-4191-7.

49. Shen, Z.T., and Sigalov, A.B. (2017). Rationally designed ligand-independent peptide inhibitors of TREM-1 ameliorate collagen-induced arthritis. J. Cell Mol. Med. *21*, 2524–2534. https://doi.org/10.1111/jcmm.13173.

50. Loftus, T.J., Mohr, A.M., and Moldawer, L.L. (2018). Dysregulated myelopoiesis and hematopoietic function following acute physiologic insult. Curr. Opin. Hematol. *25*, 37–43. https://doi.org/10.1097/MOH.0000000000000395.

51. Pietras, E.M., Mirantes-Barbeito, C., Fong, S., Loeffler, D., Kovtonyuk, L.V., Zhang, S., Lakshminarasimhan, R., Chin, C.P., Techner, J.M., Will, B., et al. (2016). Chronic interleukin-1 exposure drives haematopoietic stem cells towards precocious myeloid differentiation at the expense of self-renewal. Nat. Cell Biol. *18*, 607–618. https://doi.org/10.1038/ncb3346.

52. Sica, A., Guarneri, V., and Gennari, A. (2019). Myelopoiesis, metabolism and therapy: a crucial crossroads in cancer progression. Cell Stress *3*, 284–294. https://doi.org/10.15698/cst2019.09.197.

53. Mulder, W.J.M., Ochando, J., Joosten, L.A.B., Fayad, Z.A., and Netea, M.G. (2019). Therapeutic targeting of trained immunity. Nat. Rev. Drug Discov. *18*, 553–566. https://doi.org/10.1038/s41573-019-0025-4.

54. Bouchon, A., Facchetti, F., Weigand, M.A., and Colonna, M. (2001). TREM-1 amplifies inflammation and is a crucial mediator of septic shock. Nature *410*, 1103–1107. https://doi.org/10.1038/35074114.

55. Wu, J., Li, J., Salcedo, R., Mivechi, N.F., Trinchieri, G., and Horuzsko, A. (2012). The proinflammatory myeloid cell receptor TREM-1 controls Kupffer cell activation and development of hepatocellular carcinoma. Cancer Res. *72*, 3977–3986. https://doi.org/10.1158/0008-5472.CAN-12-0938.

56. Nguyen-Lefebvre, A.T., Ajith, A., Portik-Dobos, V., Horuzsko, D.D., Arbab, A.S., Dzutsev, A., Sadek, R., Trinchieri, G., and Horuzsko, A. (2018). The innate immune receptor TREM-1 promotes liver injury and fibrosis. J. Clin. Invest. *128*, 4870–4883. https://doi.org/10.1172/JCI98156.

57. Wu, Q., Zhou, W., Yin, S., Zhou, Y., Chen, T., Qian, J., Su, R., Hong, L., Lu, H., Zhang, F., et al. (2019). Blocking Triggering Receptor Expressed on Myeloid Cells-1-Positive Tumor-Associated Macrophages Induced by Hypoxia Reverses Immunosuppression and Anti-Programmed Cell Death Ligand 1 Resistance in Liver Cancer. Hepatology *70*, 198–214. https://doi.org/10.1002/hep.30593.

58. Liu, T., Chen, S., Xie, X., Liu, H., Wang, Y., Qi, S., Shi, L., Zhou, X., Zhang, J., Wang, S., et al. (2021). Soluble TREM-1, as a new ligand for the membrane receptor Robo2, promotes hepatic stellate cells activation and liver fibrosis. J. Cell Mol. Med. *25*, 11113–11127. https://doi.org/10.1111/jcmm.17033.

59. Dosset, M., Vauchy, C., Beziaud, L., Adotevi, O., and Godet, Y. (2013). Universal tumor-reactive helper peptides from telomerase as new tools for anticancer vaccination. OncoImmunology *2*, e23430. https://doi.org/10.4161/onci.23430.

60. Laurent, P., Allard, B., Manicki, P., Jolivel, V., Levionnois, E., Jeljeli, M., Henrot, P., Izotte, J., Leleu, D., Groppi, A., et al. (2021). TGFbeta promotes low IL10-producing ILC2 with profibrotic ability involved in skin fibrosis in systemic sclerosis. Ann. Rheum. Dis. *80*, 1594–1603. https://doi.org/10.1136/annrheumdis-2020-219748.

61. Gulati, G.S., Sikandar, S.S., Wesche, D.J., Manjunath, A., Bharadwaj, A., Berger, M.J., Ilagan, F., Kuo, A.H., Hsieh, R.W., Cai, S., et al. (2020). Single-cell transcriptional diversity is a hallmark of developmental potential. Science *367*, 405–411. https://doi.org/10.1126/science.aax0249.

62. Li, T., Fu, J., Zeng, Z., Cohen, D., Li, J., Chen, Q., Li, B., and Liu, X.S. (2020). TIMER2.0 for analysis of tumor-infiltrating immune cells. Nucleic Acids Res. *48*, W509–W514. https://doi.org/10.1093/nar/gkaa407.

63. Raudvere, U., Kolberg, L., Kuzmin, I., Arak, T., Adler, P., Peterson, H., and Vilo, J. (2019). g:Profiler: a web server for functional enrichment analysis and conversions of gene lists (2019 update). Nucleic Acids Res. *47*, W191–W198. https://doi.org/10.1093/nar/gkz369.

64. Lánczky, A., and Győrffy, B. (2021). Web-Based Survival Analysis Tool Tailored for Medical Research (KMplot): Development and Implementation. J. Med. Internet Res. *23*, e27633. https://doi.org/10.2196/27633.

65. Jin, S., Guerrero-Juarez, C.F., Zhang, L., Chang, I., Ramos, R., Kuan, C.H., Myung, P., Plikus, M.V., and Nie, Q. (2021). Inference and analysis of cell-cell communication using CellChat. Nat. Commun. *12*, 1088. https://doi.org/10.1038/s41467-021-21246-9.

66. Haeussler, M., Schönig, K., Eckert, H., Eschstruth, A., Mianné, J., Renaud, J.B., Schneider-Maunoury, S., Shkumatava, A., Teboul, L., Kent, J., et al. (2016). Evaluation of off-target and on-target scoring algorithms and integration into the guide RNA selection tool CRISPOR. Genome Biol. *17*, 148. https://doi.org/10.1186/s13059-016-1012-2.

67. Denisenko, E., Guo, B.B., Jones, M., Hou, R., de Kock, L., Lassmann, T., Poppe, D., Clément, O., Simmons, R.K., Lister, R., and Forrest, A.R.R. (2020). Systematic assessment of tissue dissociation and storage biases in single-cell and single-nucleus RNA-seq workflows. Genome Biol. *21*, 130. https://doi.org/10.1186/s13059-020-02048-6.

68. McGinnis, C.S., Murrow, L.M., and Gartner, Z.J. (2019). DoubletFinder: Doublet Detection in Single-Cell RNA Sequencing Data Using Artificial Nearest Neighbors. Cell Syst. *8*, 329–337.e4. https://doi.org/10.1016/j.cels.2019.03.003.

69. Germain, P., Lun, A., Macnair, W., and Robinson, M. (2021). Doublet identification in single-cell sequencing data using scdblfinder [version 1; peer review: 1 approved, 1 approved with reservations. F1000Research *10*. https://doi.org/10.12688/f1000research.73600.1.

70. Bais, A.S., and Kostka, D. (2020). scds: computational annotation of doublets in single-cell RNA sequencing data. Bioinformatics *36*, 1150–1158. https://doi.org/10.1093/bioinformatics/btz698.

71. Domínguez Conde, C., Xu, C., Jarvis, L.B., Rainbow, D.B., Wells, S.B., Gomes, T., Howlett, S.K., Suchanek, O., Polanski, K., King, H.W., et al. (2022). Cross-tissue immune cell analysis reveals tissue-specific features in humans. Science *376*, eabl5197. https://doi.org/10.1126/science.abl5197.

72. Patil, A., and Patil, A. (2022). Cellkb immune: a manually curated database of mammalian hematopoietic marker gene sets for rapid cell type identification. Preprint at bioRxiv. https://doi.org/10.1101/2020.12.01.389890.

73. Kolberg, L., Raudvere, U., Kuzmin, I., Vilo, J., and Peterson, H. (2020). Gprofiler2 – an R package for gene list functional enrichment analysis and namespace conversion toolset g:profiler. F1000Res *9*. https://doi.org/10.12688/f1000research.24956.2.

74. Ozisik, O., Térézol, M., and Baudot, A. (2022). orsum: a Python package for filtering and comparing enrichment analyses using a simple principle. BMC Bioinf. *23*, 293. https://doi.org/10.1186/s12859-022-04828-2.

75. Cancer Genome Atlas Research Network Electronic address wheeler@bcmedu; Cancer Genome Atlas Research Network (2017). Comprehensive and Integrative Genomic Characterization of Hepatocellular CarcinomaElectronic address, w.b.e., and Cancer Genome Atlas Research, N. Cell *169*, 1327–1341.e23. https://doi.org/10.1016/j.cell.2017.05.046.

76. Pinyol, R., Torrecilla, S., Wang, H., Montironi, C., Piqué-Gili, M., Torres-Martin, M., Wei-Qiang, L., Willoughby, C.E., Ramadori, P., Andreu-Oller, C., et al. (2021). Molecular characterisation of hepatocellular carcinoma in patients with non-alcoholic steatohepatitis. J. Hepatol. *75*, 865–878. https://doi.org/10.1016/j.jhep.2021.04.049.

77. Villanueva, A., Portela, A., Sayols, S., Battiston, C., Hoshida, Y., Méndez-González, J., Imbeaud, S., Letouzé, E., Hernandez-Gea, V., Cornella, H., et al. (2015). DNA methylation-based prognosis and epidrivers in hepatocellular carcinoma. Hepatology *61*, 1945–1956. https://doi.org/10.1002/hep.27732.

78. Chen, S., Zhou, Y., Chen, Y., and Gu, J. (2018). fastp: an ultra-fast all-in-one FASTQ preprocessor. Bioinformatics *34*, i884–i890. https://doi.org/10.1093/bioinformatics/bty560.

79. Dobin, A., Davis, C.A., Schlesinger, F., Drenkow, J., Zaleski, C., Jha, S., Batut, P., Chaisson, M., and Gingeras, T.R. (2013). STAR: ultrafast universal RNA-seq aligner. Bioinformatics *29*, 15–21. https://doi.org/10.1093/bioinformatics/bts635.

80. Ewels, P., Magnusson, M., Lundin, S., and Käller, M. (2016). MultiQC: summarize analysis results for multiple tools and samples in a single report. Bioinformatics *32*, 3047–3048. https://doi.org/10.1093/bioinformatics/btw354.

STAR★METHODS

KEY RESOURCES TABLE

REAGENT or RESOURCE	SOURCE	IDENTIFIER
Antibodies		
anti-Human CD14 (clone REA 599) APC-Vio770	Miltenyi	Cat#130-110-580; RRID: AB_2655062
anti-Human CD15 (clone HI98) BV786	BD Biosciences	Cat#563838; RRID:AB_2738444
anti-Human CD163 (clone REA812) PE-Vio770	Miltenyi	Cat#130-112-130; RRID:AB_2655485
anti-Human CD19 (clone REA675) APC-Vio770	Miltenyi	Cat#130-113-643; RRID:AB_2726196
anti-Human CD19 (clone REA675) PE-Vio770	Miltenyi	Cat#130-113-647; RRID:AB_2726200
anti-Human CD3 (clone REA613) APC-Vio770	Miltenyi	Cat#130-113-136; RRID:AB_2725964
anti-Human CD3 (clone HIT3a) PE	BD Biosciences	Cat#555340; RRID:AB_395746
anti-Human CD33 (clone REA 775) PE-Vio615	Miltenyi	Cat#130-111-026; RRID:AB_2657565
anti-Human CD36 (clone REA760) FITC	Miltenyi	Cat#130-110-739; RRID:AB_2657727
anti-Human CD4 (clone M-T466) PE-Vio770	Miltenyi	Cat#130-113-255; RRID:AB_2726057
anti-Human CD45 (clone H130) FITC	BioLegend	Cat#304054; RRID:AB_314393
anti-Human CD45 (clone REA747) Viogreen	Miltenyi	Cat#130-110-638; RRID:AB_2658245
anti-Human CD56 (clone REA196) APC-Vio770	Miltenyi	Cat#130-114-548; RRID:AB_2733136
anti-Human HLA-DR (clone REA805) FITC	Miltenyi	Cat#130-111-788; RRID:AB_2652156
anti-Human IFN-γ (clone REA600) APC	Miltenyi	Cat#130-113-495; RRID:AB_2751118
anti-Human LOX-1 (clone REA1188) APC	Miltenyi	Cat#130-122-111; RRID:AB_2784411
anti-Human TCRα/β (clone REA652) APC-Vio770	Miltenyi	Cat# 130-113-536; RRID:AB_2733169
anti-Human TNF-α (clone REA) FITC	Miltenyi	Cat#130-127-530; RRID:AB_2905444
anti-Human TREM1 (clone TREM-26) PE	BioLegend	Cat#314906; RRID:AB_389355
anti-Mouse TNF (clone MP6-XT22) FITC	BD Biosciences	Cat#554418; RRID:AB_395379
anti-Mouse CD4 (clone RM4-5) BV786	BD Biosciences	Cat#563727; RRID:AB_2728707
anti-Mouse CD8a (clone REA601) APC-Vio770	Miltenyi	Cat#130-120-737; RRID:AB_2752183
anti-Mouse CD3E (clone MP6-XT22) BB700	BD Biosciences	Cat#566495; RRID:AB_2744393
anti-Mouse CD45 (Clone 737) Viogreen	Miltenyi	Cat#130-110-665; RRID:AB_2658225
anti-Mouse TREM1 (clone 174031) BV421	BD Biosciences	Cat#747899; RRID:AB_2872361
anti-Mouse Ly-6G (clone REA 526) APC-Vio770	Miltenyi	Cat#130-119-126; RRID:AB_2733089
anti-Mouse Ly-6C (clone 796) BB700	Miltenyi	Cat#130-111-782; RRID:AB_2652815
anti-Mouse CD11b (clone REA 592) FITC	Miltenyi	Cat#130-113-243; RRID:AB_2726049
anti-Mouse CD49b (clone HMα2) BV711	BD biosciences	Cat#740704; RRID:AB_2740388
anti-Mouse CD16/CD32 (clone 93)	Thermo Fisher Scientific	Cat#14-0161-83; RRID:AB_467133
Rat anti-Mouse FoxP3 (clone FJK-16s)	Thermo Fisher Scientific	Cat#14-5773-82; RRID:AB_467576
Rat anti-Mouse CD8a (clone 4SM15)	Thermo Fisher Scientific	Cat#14-0808-82; RRID:AB_2572861
Mouse anti-Human CD163 (clone 10D6)	Invitrogen	Cat#MA5-11458; RRID:AB_10982556
Mouse anti-Human CLEC4E (clone E−5)	Santa Cryz	Cat# sc-390807L
Rabbit anti-Human TREM1	LSBio	Cat#LS-C818338
anti-Human IL10 (Clone 23738)	R&D System	Cat#MAB217; RRID:AB_358064
Mouse IgG1, Isotype control (clone MOPC-21)	BioLegend	Cat# 400102; RRID:AB_2891079
Ultra-LEAF Purified anti-mouse Gr-1 Antibody (clone RB6-8C5)	BioLegend	Cat#108453; RRID:AB_2876420
Ultra-LEAF Purified anti-mouse PD1 Antibody (clone RMP1-14)	BioLegend	Cat#114122; RRID:AB_2616682
Ultra-LEAF Purified Rat IgG2a, κ Isotype Ctrl Antibody	BioLegend	Cat#400573; RRID:AB_11148951
Goat anti-Rat Alexa 568	Invitrogen	Cat# A11077; RRID:AB_2534121
anti-Human CD15 (clone HI98) BV786	BD Biosciences	Cat#563838; RRID:AB_2738444
anti-Human CD163 (clone REA812) PE-Vio770	Miltenyi	Cat#130-112-130; RRID:AB_2655485

(*Continued on next page*)

Continued

REAGENT or RESOURCE	SOURCE	IDENTIFIER
anti-Human CD19 (clone REA675) APC-Vio770	Miltenyi	Cat#130-113-643; RRID:AB_2726196
anti-Human CD19 (clone REA675) PE-Vio770	Miltenyi	Cat#130-113-647; RRID:AB_2726200
anti-Human CD3 (clone REA613) APC-Vio770	Miltenyi	Cat#130-113-136; RRID:AB_2725964
anti-Human CD3 (clone HIT3a) PE	BD Biosciences	Cat#555340; RRID:AB_395746
anti-Human CD33 (clone REA 775) PE-Vio615	Miltenyi	Cat#130-111-026; RRID:AB_2657565
anti-Human CD36 (clone REA760) FITC	Miltenyi	Cat#130-110-739; RRID:AB_2657727
anti-Human CD4 (clone M-T466) PE-Vio770	Miltenyi	Cat#130-113-255; RRID:AB_2726057
anti-Human CD45 (clone H130) FITC	BioLegend	Cat#304054; RRID:AB_314393
anti-Human CD45 (clone REA747) Viogreen	Miltenyi	Cat#130-110-638; RRID:AB_2658245
anti-Human CD56 (clone REA196) APC-Vio770	Miltenyi	Cat#130-114-548; RRID:AB_2733136
anti-Human HLA-DR (clone REA805) FITC	Miltenyi	Cat#130-111-788; RRID:AB_2652156
anti-Human IFN-γ (clone REA600) APC	Miltenyi	Cat#130-113-495; RRID:AB_2751118
anti-Human LOX-1 (clone REA1188) APC	Miltenyi	Cat#130-122-111; RRID:AB_2784411
anti-Human TCRα/β (clone REA652) APC-Vio770	Miltenyi	Cat# 130-113-536; RRID:AB_2733169
anti-Human TNF-α (clone REA) FITC	Miltenyi	Cat#130-127-530; RRID:AB_2905444
anti-Human TREM1 (clone TREM-26) PE	BioLegend	Cat#314906; RRID:AB_389355
anti-Mouse TNF (clone MP6-XT22) FITC	BD Biosciences	Cat#554418; RRID:AB_395379
anti-Mouse CD4 (clone RM4-5) BV786	BD Biosciences	Cat#563727; RRID:AB_2728707
anti-Mouse CD8a (clone REA601) APC-Vio770	Miltenyi	Cat#130-120-737; RRID:AB_2752183
anti-Mouse CD3E (clone MP6-XT22) BB700	BD Biosciences	Cat#566495; RRID:AB_2744393
anti-Mouse CD45 (Clone 737) Viogreen	Miltenyi	Cat#130-110-665; RRID:AB_2658225
anti-Mouse TREM1 (clone 174031) BV421	BD Biosciences	Cat#747899; RRID:AB_2872361
anti-Mouse Ly-6G (clone REA 526) APC-Vio770	Miltenyi	Cat#130-119-126; RRID:AB_2733089
anti-Mouse Ly-6C (clone 796) BB700	Miltenyi	Cat#130-111-782; RRID:AB_2652815
anti-Mouse CD11b (clone REA 592) FITC	Miltenyi	Cat#130-113-243; RRID:AB_2726049
anti-Mouse CD49b (clone HMα2) BV711	BB biosciences	Cat#740704; RRID:AB_2740388
anti-Mouse CD16/CD32 (clone 93)	Thermo Fisher Scientific	Cat#14-0161-83; RRID:AB_467133
Rat anti-Mouse FoxP3 (clone FJK-16s)	Thermo Fisher Scientific	Cat#14-5773-82; RRID:AB_467576
Rat anti-Mouse CD8a (clone 4SM15)	Thermo Fisher Scientific	Cat#14-0808-82; RRID:AB_2572861
Mouse anti-Human CD163 (clone 10D6)	Invitrogen	Cat#MA5-11458; RRID:AB_10982556
Mouse anti-Human CLEC4E (clone E−5)	Santa Cryz	Cat#sc-390807L
Rabbit anti-Human TREM1	LSBio	Cat#LS-C818338
anti-Human IL10 (Clone 23738)	R&D System	Cat#MAB217; RRID:AB_358064
Mouse IgG1, Isotype control (clone MOPC-21)	BioLegend	Cat# 400102; RRID:AB_2891079
Ultra-LEAF Purified anti-mouse Gr-1 Antibody (clone RB6-8C5)	BioLegend	Cat#108453; RRID:AB_2876420
Ultra-LEAF Purified anti-mouse PD1 Antibody (clone RMP1-14)	BioLegend	Cat#114122; RRID:AB_2800575
Ultra-LEAF Purified Rat IgG2a, κ Isotype Ctrl Antibody	BioLegend	Cat#400573; RRID:AB_11148951
Goat anti-Rat Alexa 568	Invitrogen	Cat#A11077; RRID:AB_2534121
Biological samples		
HCC and adjacent non-tumoral liver	Department of Oncology, Haut Leveque Hospital, Pessac, France	See Table S1 for details
Chemicals, peptides, and recombinant proteins		
GF9 peptide	Genentech	GLLSKSLVF
Control peptide	Genentech	GLLSGSLVF
UCP4 TERT Peptide	Eurofin	SLCYSILKAKNAGMS
Recombinant Human IL-6	Miltenyi	Cat#130-093-929
Recombinant Human GM-CSF	Miltenyi	Cat#130-093-862

(*Continued on next page*)

Continued

REAGENT or RESOURCE	SOURCE	IDENTIFIER
Phorbol 12-myristate 13-acetate	Sigma-Aldrich	Cat#79346
Ionomycin	Sigma-Aldrich	Cat#I0634
rhPGLYRP1/PGRP-S	R&D system	Cat#2590-PGB-050
PGN-SA	Invivogen	Cat#tlrl-pgns2
Propylene glycol	Thermo Fisher Scientific	Cat#158720010
Isopentane RE	Carlo Erba	Cat#528492
Critical commercial assays		
Red Blood Cell Lysis Buffer	Merck	Cat#11814389001
GentleMACS C tubes	Miltenyi	Cat#130-096-334
Tumor Dissociation Kit, human	Miltenyi	Cat#130-095-929
RPMI Medium 1640 (1X)	GIBCO	Cat#22400071
DMEM Medium High Glucose	GIBCO	Cat#41965-09
DPBS without calcium without magnesium	Fisher Scientific	Cat#12559069
CO2 Independent medium	Fisher Scientific	Cat# 11580536
X-VIVO15 medium	Lonzo	Cat#BE02-060Q
Bovine Serum Albumin Fraction V (7.5%)	Fisher Scientific	Cat#11500496
EDTA 0.5 M UltraPure, pH 8.0	Fisher Scientific	Cat#15575020
Penicillin/Streptomycin	Fisher Scientific	Cat#11556461
Matrigel high concentration	BD Biosciences	Cat#354262
Sytox blue viability dye	Fisher Scientific	Cat#10482112
Viobility 405/452 Fixable Dye	Miltenyi	Cat#130-110-205
BD HorizonTM Fixable Viability Stain 700	BD Biosciences	Cat#564997
7-Amino-Actinomycin D (7AAD)	BD Biosciences	Cat#559925
Opal 4-Color Manual IHC Kit	Akoya	Cat#NEL810001KT
Prolong Gold Antifade mountant	Thermo Fisher Scientific	Cat#P36930
Spectral DAPI solution	Akoya	Cat#FP1490A
10X AR9 buffer	Akoya	Cat#AR900250ML
OPAL 520	Akoya	Cat# FP1487001KT
OPAL 650	Akoya	Cat#FP1488001KT
Cell strainer 40μm	Corning	Cat#431750
Cell strainer 70μm	Corning	Cat#352350
Trypan blue solution	Sigma-Aldrich	Cat#T8154
Chromium i7 Multiplex Kit, 96 reactions	10x Genomics	Cat#120262
Chromium Next GEM Chip G Single Cell Kit	10x Genomics	Cat#1000120
Chromium Next GEM Single Cell 3′ GEM, Library & Gel Bead Kit v3.1	10x Genomics	Cat#1000121
Bluing Buffer	Agilent	Cat#CS70230-2
Hematoxylin, Mayer's	Agilent	Cat#S30930-2
Eosin Y solution, aqueous	Merck	Cat# HT110219
Sodium dodecyl sulfate (SDS) solution, 10% in water	Merck	Cat# 71736
Visium Spatial Gene Expression Starter Kit	10x Genomics	Cat#1000200
Dual Index Kit TT Set A 96 rxns	10x Genomics	Cat#1000215
BSA Ultra Pure	Fischer Scientific	Cat#10743447
Methanol	Sigma-Aldrich	Cat#34860
Acetic Acid >99.9%	Sigma-Aldrich	Cat#A6283
Low TE Buffer	Fischer Scientific	Cat#12090-015
SSC Buffer 20x Concentrate	Sigma-Aldrich	Cat#S66391L
Potassium hydroxide solution volumetric, 8.0 M KOH	Sigma-Aldrich	Cat#P4494

(*Continued on next page*)

Continued

REAGENT or RESOURCE	SOURCE	IDENTIFIER
Hydrochloric acid solution volumetric, 0.1 M HCl	Sigma-Aldrich	Cat#2104
10% Tween 20	Biorad	Cat#1662404
Tris (1M) pH 7.0	Thermo Fisher Scientific	Cat#AM9850G
SPRISelect Reagent	Beckman Coulter	Cat#B23318
Fixation/Permeabilization Solution Kit with BD GolgiPlug	BD Biosciences	Cat#555028
16% Formaldehyde (W/V)	Fisher Scientific	Cat#11586711
RNeasy Minikit	Qiagen	Cat#74104
RNeasy Plus Micro Kit	Qiagen	Cat#74034
QIAshreader	Qiagen	Cat#79656
GoScriptTM reverse transcription system	Promega	Cat#A5001
GoTaq® qPCR Master Mix	Promega	Cat#A6001
O.C.T. Compound	VWR	Cat#361603E
DNA LoBinding Tubes, 1.5 mL	Eppendorf	Cat#022431021
Irradiated MCD-Diet AIN-76	SAFE	Cat#v248
DNAse I	Sigma-Aldrich	Cat#DN25
Collagenase IV	Sigma-Aldrich	Cat#C5138
Human pan T cell isolation kit	Miltenyi	Cat#130-096-535
Dynabeads human T-activator CD3/CD28	Gibco	Cat#11131D
Human $CD14^+$ cell isolation kit	Miltenyi	130-050-201
Human IL-10 ELISA Duoset	R&D system	Cat#DY217B-05
Human sTREM1 ELISA Quantikine	R&D system	Cat#DTRM10C
CellTrace Violet system	Thermo Fisher Scientific	Cat#C34571
Deposited data		
scRNA-seq raw and processed data (20 samples)	This paper	GEO:GSE245906
Spatial Visium raw and processed data (2 samples)	This paper	GEO:GSE245908
Bulk RNA-seq raw and processed data (9 samples)	This paper	GEO:GSE245905
Human reference genome NCBI build 38, GRCh38	Genome Reference Consortium	http://www.ncbi.nlm.nih.gov/projects/genome/assembly/grc/human/
Experimental models: Cell lines		
Murine: Hep55.1C cells	CLS	Cat#400201
Human: TERT-specific $CD4^+$ T cell clone	Dosset et al.[59]	N/A
Human: Fibroblasts	Laurent et al.[60]	N/A
Experimental models: Organisms/strains		
Mouse: C57BL/6J SPF	Charles River	Cat#632
Oligonucleotides		
sgRNA#5 target for TREM1	Integrated DNA Technology	5′-GTTCGATCGCATCCGCTTGG-3′
sgRNA#6 target for TREM1	Integrated DNA Technology	5′-CAGCTCGGAGTTCTATAAGC-3′
Primers for *COL1A1*, *RPLO*, *18S*, *TGFB1*, *TIMP1*, *TREM1* and *IL10*	This paper	See STAR Methods details for primer sequence
Software and algorithms		
Biorender	N/A	https://www.biorender.com/
DIVA	BD Biosciences	https://www.bdbiosciences.com/en-fr
FlowJo v.10.5.3	FlowJo	https://www.flowjo.com
NDP View2	Hamamashu	https://www.hamamatsu.com
GraphPad Prism 9	GraphPad	https://www.graphpad.com/scientific-software/prism/
Adobe Illustrator	Adobe	www.adobe.com

(*Continued on next page*)

Continued

REAGENT or RESOURCE	SOURCE	IDENTIFIER
CellRanger v6.0.0	10X Genomics	https://support.10xgenomics.com/single-cell-gene-expression/software/overview/welcome
SpaceRanger v1.3.0	10X Genomics	https://support.10xgenomics.com/single-cell-gene-expression/software/overview/welcome
R 4.0.0	The R core Team	https://www.r-project.org
CellTypist	Domínguez Conde et al.[71]	https://github.com/Teichlab/celltypist
BBrowser BioTuring	https://www.biorxiv.org/content/10.1101/2020.12.11.414136v1	https://bioturing.com/bbrowser
Python 3.6	Python Software Foundation	https://www.python.org
CytoTRACE	Gulati et al.[61]	https://cytotrace.stanford.edu/
CIBERSORTx	Steen et al.[42]	https://cibersort.stanford.edu/
TIMER2.0	Li et al.[62]	http://timer.cistrome.org/
g:Profiler	Raudvere et al.[63]	https://biit.cs.ut.ee/gprofiler/gost
Kaplan-Meier plotter	Lanczky et al.[64]	https://kmplot.com/analysis/
CellChat v2 R package	Jin et al.[65]	http://www.cellchat.org/
Other		
NanoZoomer 2.0HT	Hamamatsu	N/A

RESOURCE AVAILABILITY

Lead contact

Further information and requests for resources and reagents should be directed to and will be fulfilled by the lead contact Dr. Maya Saleh (maya.saleh@inrs.ca).

Materials availability

This study did not generated new unique reagents.

Data and code availability

- Single-cell RNA-seq, spatial transcriptomic and bulk RNA-seq data have been deposited at GEO with accession number GSE245909 and are publicly available as of the date of publication. Subseries accession numbers are listed in the key resources table.
- This paper does not report original code.
- Any additional information required to reanalyze the data reported in this paper is available from the lead contact upon request.

EXPERIMENTAL MODEL AND STUDY PARTICIPANT DETAILS

Study participants

The adjacent non-tumoral (NT) and tumoral (HCC) tissues were obtained from patients undergoing liver resection surgery at the Haut Leveque Hospital (Pessac, France). The patients sex (9 men and 1 woman), age range in years (60–85) and detailed clinical characteristics are summarized in Table S1. Gender information was not provided. Patients were informed about the secondary use of their data and their tissue samples for research purposes, and gave consent. This study was approved by the Health and Research Ethics Center of Bordeaux (reference CER-BDX 2024 - 10).

Animal models

The mice used in this study were male C57BL/6J purchased from Charles River at 8–10 weeks of age. Mice were housed under specific pathogen-free conditions at the animal facility at Pessac (University of Bordeaux). All experimental procedures were approved by the local ethical committee in accordance with the regulations of the French ministry. Mice were housed in a controlled environment with specific pathogen free conditions of 20°C–22°C, 12 h light/12 h dark cycle, 50–70% humidity. The food and water were provided *ad libitum*. Mice were randomly assigned to experimental groups and conditions before starting experiments.

Cell culture

Hep55.1C murine syngenic cell-line was obtained from the CLS Collection and grown in DMEM, high glucose, GlutaMAX Supplement, pyruvate (Fisher 11594446) supplemented with fetal bovine serum (FBS, 10%) and penicillin/streptomycin (1%). UCP4-specific $CD4^+$ T cells were cultured as previously reported.[59] Fibroblasts were obtained from skin reduction mammoplasties and were isolated and cultured according to.[60] Human peripheral blood mononuclear cells were isolated from blood donors at the local Blood transfusion center (University Hospital, Bordeaux, agreement n°16PLER023). All cell-lines were grown at 37°C in a humidified chamber with 5% CO2 and regularly tested as negative for mycoplasma.

METHOD DETAILS

Generation of HuMoSCs

HuMoSCs were generated according to a published protocol.[35] Briefly, healthy donor PBMC were obtained from buffy coats by the means of Ficoll density gradient centrifugation. Monocytes were then isolated from PBMC by magnetic cell sorting (human $CD14^+$ cell isolation kit; Miltenyi Biotec, 130-050-201). HuMoSCs were generated by incubating monocytes (1.10^6 cells/mL) in RPMI 1640 supplemented with 10% FBS, 1% glutamine, pyruvate, HEPES, non-essential amino acid and recombinant human GM-CSF (10 ng/mL; Miltenyi Biotec, 130-093-862) and IL-6 (10 ng/mL; Militenyi Biotec, 130-093-929) for 7 days. Sixty percent of the medium was replaced every 3 days. PGN/PGLYRP1 complex (2 μg/mL and 1 μg/mL, respectively) or water were added in the HuMoSC medium on day 6 for 24 h sTREM1and IL-10 were quantified in the medium of HuMoSC cultures on day 7. Neutralizing anti-IL10 (Clone 23738) or isotype CT (clone MOPC-21) was added in the HuMoSC medium at day 6, and 15 min before PP treatment for 24 h.

CRISPR/Cas9 mediated TREM1 Knock-out

Two sgRNA target DNA sequences were designed using CRISPOR algorithm (crispor.tefor.net;[66]) to target the *TREM1* gene. Corresponding Alt-R-crRNA was purchased from Integrated DNA Technologies (IDT) as well as human crRNA negative control and human crRNA positive control targeting the *HPRT* gene (IDT:1072541) and suspended to 200 μM in TE buffer. They were then equally mixed with 200 μM Alt-R-tracrRNA (IDT), annealed by heating for 5 min at 95°C and cooled to room temperature (RT). These dual gRNA were individually mixed with 10 μg of Alt-R S.p-Cas9HIFIv3 (IDT) with a 1.6 ratio of gRNA/Cas9. After 10 min at RT, 2.5 to 2.8 millions monocytes washed in PBS and suspended in 20μL Lonza P3 solution containing 1 μL of electroporation enhancer (IDT) were added to the CRISPR mix. Program EA-100 of the 4D-Nucleofector (Lonza) was applied. Cells were then harvested in 2 mL medium and plated in 12 wells plates.

Human tissue dissociation

The tissues were collected in CO_2 independent medium (Fisher Scientific, Cat# 11580536) and kept on ice until processing within 1 h. One histological slice was fixed in 10% buffered formalin phosphate (Sigma) and paraffin-embedded. HES- and Masson's Trichrome-stained slides were reviewed by a pathologist (Figure S1). The other slice was embedded in OCT (VWR) and put in a bath of isopentane placed in a liquid nitrogen bath. The OCT-embedded tissue blocks were stored in a sealed container at −80°C until cryo-sectioning. The last tissue was rinsed in RPMI, transferred to a sterile 60 mm^2 tissue culture dish and cut in <2 mm^3 pieces. Tissue pieces were placed in Gentle MACS C tubes and incubated in tissue dissociation solution (tumor dissociation kit, Miltenyi) using the GentleMACS dissociator (program h_TDK_2, Miltenyi). After a first step of centrifugation at 400 xg for 8 min at 4°C, dissociated cells were passed through a 40 μm filter, rinsed with complete RPMI and centrifuged at 400 xg for 5 min at 4°C. After a treatment with 5 mL red blood cell lysis (Roche) at 4°C for 5 min, cells were washed twice with PBS 2 mM EDTA 0.1% BSA (named FACS buffer) prior to counting in Trypan blue exclusion dye.

Flow cytometry staining

Dissociated cells were incubated with cell surface antibodies in FACS buffer for 25 min at 4°C in the dark or for 15 min at room temperature and washed twice before analysis. For intracellular staining of cytokines, cells were fixed and permeabilized with Fixation/Permeabilization Solution Kit according to manufacturer instructions (BD Biosciences). Viable cells were analyzed based on side scatter and viability dye. Acquisition was performed on the BD LSRFortessa. Cells from murine samples were blocked in anti-mouse CD16/32 antibody (1:200e) for 10 min at 4°C prior to addition of cell surface antibodies.

Single-cell FACS sorting

Doublet cells were double-excluded in width against forward scatter and side scatter. For scRNA-seq experiments, freshly dissociated single-cell suspensions were sorted based on this gating: FITC-$CD45^+$, APC Vio770-panTCR$\alpha\beta^-$ and PE Vio770-$CD19^-$ cells. For the immunosuppression experiments, dissociated tumor single-cell suspensions were thawed in complete RPMI medium and incubated for 10 min at 37°C to wash out residual DMSO in media. Cells were pelleted and suspended in cold FACS buffer prior to staining with cell surface antibodies: Viogreen-$CD45^+$ APC Vio770-Lin^- (CD3, CD19, CD56) FITC-$CD36^+$ PE-Vio770-$CD163^{+/-}$ APC-LOX-$1^{+/-}$. Viable cells were analyzed based on side scatter gates and Sytox blue viability dye 1:5000 (Fisher Sci.). Cells were sorted using FACS Aria II upgraded at 4°C in pre-coated (2 h at 37°C with PBS 10% FCS) 1.5 mL low binding tubes (Eppendorf)

containing either PBS-0.04% pure BSA (for scRNA-seq experiments) or complete RPMI (for co-culture experiments). Sorted cells were centrifuged at 350 xg at 4°C for 5 min and counted with trypan blue dye before being processed.

scRNA-seq

15.000 single CD45$^+$panTCR$\alpha\beta^-$CD19$^-$ innate immunity cells were loaded into a chip to form Gel Bead-in-Emulsion in the Chromium Controller. Single-cell libraries were generated using the Single Cell 3′ reagent Kit v3.1 (10X Genomics) as per the manufacturer's protocol. cDNA was amplified by 12 PCR cycles and 12 cycles were also performed for library preparation (single index PCR). Libraries were pooled and sequenced on a NovaSeq 6000.

Visium spatial gene expression processing

OCT-embedded tissue blocks were sectioned at 10μm thickness using Cryostar NX70 (Leica) and tumoral tissues containing RNA with a RIN $\geq$7 were included in the Visium experiments. One section per patient was cut at 10μm thickness and placed on Visium slide capture area (10x Genomics). Slides were then processed following the 10x Genomics Visium Spatial protocol according to the manufacturer recommendations. The slides containing tissues were methanol-fixed at −20°C and processed for H&E staining and imaging. The slides were scanned using a Nanozoomer 2.0 HT (Hamamatsu Photonics France) using objective UPS APO 20X NA 0.75 combined with an additional lens 1.75X. Virtual slides were acquired with a TDI-3CCD camera. Based on tissue optimization experiments performed on HCC#20, HCC tissues were permeabilized for 12 min. cDNA was amplified by 14 PCR cycles and 14 cycles were also performed for library preparation (dual index PCR). Libraries were pooled and sequenced on a NovaSeq 6000.

Co-culture experiments

For the immunosuppression experiment, myeloid cells sorted from from HCC surgical resections were pre-incubated for 4 h in round bottom 96-well plates with a TERT-reactive CD4$^+$ T lymphocyte clone at a ratio of 5:1 and then stimulated for 12 h with UCP4 TERT peptides plus BD Golgi Plug each at 1 μg/mL final concentration. For the control, T cells were stimulated with Phorbol 12-myristate 13-acetate at 12.5 ng/mL and ionomycin at 0.5 μg/mL (Sigma). In others immunosuppression experiments with either myeloid cells sorted from HCC surgical resections or with HuMoSCs, total T lymphocytes were purified from healthy donor PBMC from buffy coats by the means of magnetic cell sorting using human pan T cell isolation kit according to manufacturer's procedure (Miltenyi Biotec; 130-096-535). The obtained T cells were then activated with anti-CD3/CD28-coated beads (Dynabeads, Life Technologies, 11131D) and co-cultured with or without myeloid cells at different ratios (T cell/HuMoSC ratio = 1:1, 1:4). In both immunosuppression tests, cells were pelleted and suspended in FACS buffer prior to staining with cell surface antibodies (CD4-PE Vio770 and CD3-APC-Vio770) solution containing fixable viability dye. After washing, fixation and permeabilization, intracellular staining with antibody against IFNγ-APC and TNFα-FITC was performed using BD fixation/Permeabilization solutions as per the manufacturer's recommendations (BD Biosciences). The % inhibition of T cell activity was calculated as: [(%TNFα^+ CD4$^+$/or CD8$^+$ T cell in the positive control stimulation i.e., with the TERT-derived peptide or with anti-CD3/CD28 antibodies) − (% TNFα^+ CD4$^+$/or CD8$^+$ T cell in the other tested wells) × 100]/(% TNFα^+ CD4$^+$/or CD8$^+$ T cell in the positive control stimulation). In the proliferation assay, T cells were stained with CellTrace Violet Dye (Thermo Fisher Scientific Cat# C34571) according to the manufacturer's recommendations and then activated with anti-CD3/CD28-coated beads with or without HuMoSCs (ratio 3:1). After 6 days of co-culture, proliferation of CD3$^+$ T cells was analyzed by flow cytometry after CD3-PE staining and addition of viability dye (7AAD).

MCD-diet mouse model

7-weeks old C57BL/6J male mice were fed a Methionine- and Choline-Deficient (MCD) diet from week 7 to week 11.5. The diet was halted 9 days between weeks 9.3 and 10.7. Tumor cells were implanted in the liver at week 10 and mice were sacrificed at 13-week of age and tumors were recovered.

Orthotopic tumor injection and tumor growth monitoring

10-weeks old C57BL/6J male mice were treated with buprenorphine s.c. at 0.1 mg/kg 30 min prior to anesthesia with isoflurane (2L/min oxygen). Laparotomy was done to expose the left lateral liver lobe and 20μL of Hep55.1C cells (0.25 x 10^6 cells) in Matrigel (7 mg/mL) suspension was gently injected under the liver capsule. A sterile Gel foam was placed on the needle track for 2 min to prevent leakage of cells. Mice were treated with GF9 or control peptide at 25 mg/kg (in 20% propylene glycol, 10% ethanol and 2% Tween 80, i.p. injection) three times a week from day 8 post inoculation of cells till sacrifice. Mice were treated with anti-Gr1 (BioLegend Cat# 108453), anti-PD1 (BioLegend Cat# 114122) or isotype control (BioLegend Cat# 400573) (i.p. injection, 200μg per mice) two times a week from day 8 till sacrifice. For anti-Gr1 treatment, mice were injected a first dose of 400μg antibodies. Tumor growth was monitored using bioluminescence on isoflurane anesthetized mice.

Mouse tumor dissociation

Mouse tumors were dissociated in Gentle MACS C tubes containing RPMI medium supplemented with 1% glutamine, 1% P/S, 50 μL/mL DNAse I and 1 mg/mL collagenase IV for 45 min at 37°C under agitation. C tubes were run in GentleMACS dissociator before and after incubation (program mLiver_3, Miltenyi). After a first step of centrifugation at 400 xg for 8 min at 4°C, dissociated cells were passed through a 70μm filter, rinsed with complete RPMI and centrifuged at 400 xg for 5 min at 4°C. After a treatment

with 1mL ACK buffer (Gibco) at room temperature (RT) for 5 min, cells were washed twice with FACS buffer and processed for flow cytometry.

Immunofluorescence and multiplex Immunohistochemistry staining and imaging

3μm-thick formalin-fixed paraffin-embedded tissue sections were placed at 37°C overnight and then for 1h at 60°C. The slides were deparaffinized in fresh xylene and rehydrated in decreasing concentrations of ethanol. The slides were immersed in AR9 buffer, placed in a jar and heated in a microwave for 180 s at 1000 mw until the buffer boils, followed by an additional microwave treatment for 30 min at 160 mw. Slides were allowed to cool down for 30 min at room temperature, rinsed with PBS and blocked in PBS 10% FCS and 1% BSA for 30 min at room temperature. Primary antibody diluted in PBS 10% FCS (CD8a, 1:400e; FoxP3, 1:100) were incubated 1 h at 37°C. After washing twice in PBS, secondary antibody (Alexa 568, 1:300e) was incubated at room temperature for 30 min. Multiplex IHC was performed according to manufacturer' recommendation (Akoya). Primary antibodies (CLEC4E, 1:200e; CD163, 1:100; TREM1, 1:250) were incubated 1.5 h at RT and OPAL 520 or OPAL 650 were used at 1/200e. Slides were counterstained with spectral DAPI (Akoya) and mounted with Prolong Antifade Mountant (Thermofisher scientific). The tissue imaging was done at the Bordeaux Imaging Center, a service unit of the CNRS-INSERM and Bordeaux University, member of the national infrastructure France BioImaging supported by the French National Research Agency (ANR-10-INBS-04). The slides were scanned using Hamamatsu NANOZOOMER 2.0HT and images were taken using objective 40X. For quantification, fluorescent objects in both channels within a fixed ROI were counted. Five ROI per mouse and 3 mice per treatment were quantified.

RNA extraction and RT-qPCR

RNA was isolated from fibroblasts or HuMoSC using the RNeasy Plus Mini Kit (Qiagen) according to the manufacturer's protocol. 100 ng of RNA was reverse transcribed (Promega) and qPCR was performed in duplicate in 384-well plate format using GoTaq qPCR Master mix with primers for human *COL1A1* (Forward [F]: 5′CCCTCCTGACGCACGG3'; Reverse [R]: 5′GTGATTGGTGGGATGTCTT3′), *TGFB1* (F: 5′CTAATGGTGGAAACCCACA3'; R: 5′TATCGCCAGGAATTGTTGC3′), *TIMP1* (F: 5′CGTTATGAGATCAAGATGA3'; R: 5′CCCCTAAGG CTTGGAACCC3′), *TREM1* (F: 5′GCAGCCAGAAAGCTTGGCAGATAA3'; R:5′ATCCACCAGCCAGGAGAATGACAA3′) or *IL10* (F: 5′GAC TTTAAGGGTTACCTGG3'; R: 5′TCACATGCGCCTTGATGTC3′). The 2-ΔΔCt quantification method using *RPL0* (F: 5′GCAGCATCTA CAACCCTGA3'; R: 5′CACTGGCAACATTGCGGAC3′and *18S* (F: 5′TGCCATCACTGCCATTAAG3'; R: 5′ TGCTTTCCTCAACACCA CAT3′) primers for normalization, was used to calculate the average mRNA expression levels.

Transcriptomic analyses of sorted innate immune cells and sorted THBS1^{+} myeloid cells – Sample preparation

Innate immune cells from six patients: HCC#17, HCC#18, HCC#19, HCC#20, HCC#23 and HCC#24 were isolated using the same sorting strategy designed for scRNA-seq experiments. THBS1^{+} M subsets were isolated according to the sorting strategy in Figure S3E. Viability and single cells were verified under microscope and cells were immediately lysed in RNA extraction buffer and stored at −80°C. Sorted THBS1^{+} M cells from five HCC patients were pooled and RNA were extracted using the RNeasy Plus Micro Kit (Qiagen). Libraries were constructed using Low Input Library Prep Kit (TakaraBio) and sequenced on a NovaSeq 6000 with a run configuration of 2 × 150 bp.

scRNA-seq data processing, quality control and cleaning

A data processing summary is presented in Figure S1C and Table S2. Each of the 10X Chromium single-cell Gene Expression data were pre-processed using CellRanger software 6.0.0, including demultiplexing, reads alignment on human reference genome assembly GRCh38 (refdata-gex-GRCh38-2020-A), barcoding and counting of unique UMI. Raw UMI count matrices were imported in R environment to perform deeper quality control steps to exclude low-quality cells. Cells containing less than 300 or more than 4,500 detected features and cells with more than 40,000 counts were discarded. Moreover, cells expressing more than 12% of mitochondrial genes or more than 15% of ribosomal genes were eliminated. A supplementary criteria was added to exclude stressed cells based on a stress response score.[67] The stress response score was calculated using AddModuleScore function from Seurat package (version 4.0.1) with the following list of genes: *FOSB*, *FOS*, *JUN*, *JUNB*, *JUND*, *ATF3*, *EGR1*, *HSPA1A*, *HSPA1B*, *HSP90AB1*, *HSPA8*, *HSPB1*, *IER3*, *IER2*, *BTG1*, *BTG2*, *DUSP1*.

Cell doublet detection and removal

Three different doublet predictions were performed using DoubletFinder (version 2.0.3),[68] scDblFinder (version 1.7.7)[69] and scds (version 1.8.0).[70] A consensus method was applied, i.e., a cell was considered as a multiplet and discarded if identified in at least two of the three methods. On average, doublets were estimated at around 4%, ranging from 1% (sample with the lowest number of cells) to 5.8%. Cleaning and doublets removal account for 10 to 47% of the cells retrieved with CellRanger. Total recovery ranges from 11 to 49% (Table S2).

Normalization and data integration

The 20 pre-processed scRNA-seq data (10 adjacent non-tumoral and 10 tumoral) were normalized using SCTransform (version 0.3.2) with method = «glmGamPoi » before integration. Functions PrepSCTIntegration with 3,000 features, FindIntegrationAnchors with dims = 30, reduction = «rpca» and reference (4 samples) options, and IntegrateData from Seurat were used to integrate all 20 samples.

Unsupervised clustering, dimensionality reduction and data visualization

Unsupervised clustering, dimensionality reduction and most visualization were performed with Seurat (version 4.0.1). RunPCA function was used with 30 dimensions. The optimized number of dimensions used for RunTSNE and RunUMAP functions was automatically calculated with an in-house script. FindNeighbors and FindClusters (res = 0.5) function were used to predict the 22 clusters described in the main text. FindAllMarkers (min.pct = 0.25, logfc.threshold = 0.25) function was used to identify discriminating features between clusters.

Cell type/state annotation

Automatic and manual methods were combined to annotate as precisely as possible cell types or states: (1) expression of canonical markers were visualized and lists of discriminating markers were first manually investigated; (2) lists of markers were downloaded from Panglao database, a score method was applied using AddModuleScore and results were visualized on FeaturePlots; and (3) automatic predictions were done using CellTypist[71] with the whole dataset and cellKB software[72] using discriminating lists of markers as input.

Identification of signature genes

We defined gene signatures as the minimal number of genes allowing to discriminate a cluster from others. Top 20 discriminating genes were investigated and adjusted as necessary to refine the signatures. To validate signatures, scores were calculated using AddModuleScore and visualized using VlnPlot and FeaturePlot functions from Seurat on the different datasets. Signature specificity was calculated as the mean expression of a marker gene in a test cluster divided by the mean expression of the same gene in the cluster that expresses it at its second highest level.

Phylogenetic relationships of clusters based on gene expression

To investigate relationships between THBS1^{+} monocytes and other myeloid clusters, we removed the pDC and CYT clusters from the MNP set, and merged it with Neutro_c12 (from the innate immune dataset). We, then, selected the top 500 Highly Variable Features based on standardized variance using HVFInfo from Seurat. Finally, we used the two BuildClusterTree and PlotClusterTree functions from Seurat.

Trajectory inference

Trajectory analyses were performed using monocle (version 2.20.0) and slingshot (version 1.6.1) R packages. A reduced number of cells (n = 300) was used to increase the speed of calculation using subset function from Seurat option downsample. Differentially and temporally expressed genes were identified using differentialGeneTest function with options fullModelFormulaStr = '∼Cluster' and fullModelFormulaStr = "∼sm.ns(Pseudotime)", respectively.

RNA velocity estimation

Using bam files from CellRanger, we generated loom files using Velocyto pipeline 63 with velocyto run10x. We merged loom files of the 20 samples using loompy python package from Linnarsson Lab. We then imported the combined loom files into R and added the ''spliced'', ''unspliced'' and ''ambiguous'' assays into our pre-existing Seurat object. We normalized the ''spliced'' assay using SCTransform. Velocity estimations were calculated using RunVelocity function from Velocyto.R in SeuratWrappers. Finally, we used show.velocity.on.embedding.cor function with the UMAP embedding to visualize the average velocity of nearby cells.

Estimation of differentiation potency or signaling entropy

The differentiation potency of single-cells was estimated using the SCENT package 29, with the provided functional gene network « net13Jun12». Normalized count matrices were log(x + 1) transformed. Signaling Entropy Rates (SR) were calculated using Correlation of Connectome and Transcriptome (CCAT) 30 with CompCCAT function, implemented in SCENT. High values indicate higher potency or signaling promiscuity/entropy (capacity to differentiate to different lineages). Furthermore, we predicted differentiation states using CytoTRACE 64. We downsampled MNP sets by using 200 cells per cluster and used the online version of CytoTRACE.

Differential expression analysis, gene ontology and gene set enrichment analysis

Differential gene expression between two clusters or between two conditions were performed using FindMarkers function from Seurat. Gene Ontology and enrichment analyses were done using gprofiler.[73] Filtering and visualization were done using orsum python package.[74]

Pre-processing and visualization of spatial transcriptomic data

Spatial data were pre-processed and aligned using SpaceRanger software v1.3.0 with the reference human genome GRCh38 (refdata-gex-GRCh38-2020-A) to generate raw UMI count spot matrices. Raw UMI counts were normalized using SCTransform. Dimensionality reduction was performed using classical PCA and clustering was performed using Louvain clustering with FindNeighbors and FindClusters functions, as before. Signatures were spatially visualized using AddModuleScore function. Gene expression visualizations were generated using BBrowser BioTuring (Le et al. https://www.biorxiv.org/content/10.1101/2020.12.11.414136v1).

Spatial co-occurrence analysis

To investigate cell type co-occurence in spatial transcriptomics, we used AddModuleScore function with cell type related signatures. We selected spots based on quantiles over a 0.9 probability as top spots scoring positive for each signature, and then defined co-localization (spots positive for two or more signatures). We used linear regression and Pearson's Chi-square (X2) to test the number of spots significantly enriched in multiple populations in both fibrotic and non-fibrotic regions of HCC. Fibrotic regions were also defined using the signature method.

Cell-cell communication analysis

To predict communication between THBS1$^+$ M populations and CAF populations, we used CellChat v2 R package.[65] We used a subset of our MNP set including THBS1$^+$ M, monocytes and macrophages. To investigate interactions with fibroblasts, we downloaded the processed count data from Qi et al.[41] and only kept fibroblast populations. We used *NormalizeData*() function from Seurat package to normalize the fibroblast set before merging them with our MNP. We created a CellChat object and used the CellChatDB.human database. Default parameters were used with ''triMean'' average computation.

Transcriptomic source data of external cohorts

To validate the tissue distribution of MNP subsets and their association with clinical parameters, we interrogated several large cohorts of patients with HCC. We used the LIHC TCGA cohort (https://www.cancer.gov/tcga). Normalized count tables were downloaded using TCGAbiolinks R package 65 with GDCquery function and the following options: data.category = «Gene expression», data.type = «Gene expression quantification», platform = «Illumina HiSeq», file.type = «normalized_results». Clinical data with patient overall survival durations and tumor grades were downloaded with the GDCquery_clinic function. Supplementary clinical information of 196 patients of the LIHC cohort were retrieved from The Cancer Genome Atlas Research Network.[75] We also used a second cohort of tumor and adjacent non-tumor tissues from hepatocellular carcinoma, GSE76427.[43] Finally, we specifically investigated NASH and non-NASH HCC tumors using GSE164760 [76] and GSE63898 [77] cohorts. For these three latter cohorts, we used the GEOquery R library to download the data.

Immuno-deconvolution and cancer genomics

We estimated proportions of scRNA-seq cell subsets in the previously cited external cohorts using CIBERSORTx.[42] We used our MNP dataset. To extract the normalized count matrix, we downsampled the number of barcodes to 200 per cell type for our MNP subsets. We built scRNA-seq signature matrices in CIBERSORTx web server. We imputed cell fractions of each immune set within each cohort described in the previous section, with option S-mode 'Batch correction'. Parsing and visualizations of the proportions were then realized using tidyverse, reshape2, ggplot2, ggsignif, pheatmap, cowplot and corrplot R packages. We performed survival analyses using survminer and survival R packages. Moreover, we verified CIBERSORTx signatures for each cell-type based on signature scoring from file 'sig_inferred_refsample.bm.K999.txt'. We extracted top-scored 100 genes per cluster. This allowed us to validate our manual signatures to identify highly specific genes.

Transcriptomic analyses of sorted innate immune cells and sorted THBS1+ monocytes – data processing and analysis

To validate the transcriptomic programs of the three THBS1$^+$ myeloid populations (c0, c3, c4), we analyzed at the bulk transcriptomic level the three sequenced samples. Quality checks of the Fastq files were done using fastp 0.23.2.[78] Mapping and counting were realized using STAR 2.7.10a[79] on the human genome (Gencode v44). Mapping results were then visualized and summarized using multiQC 1.11 software.[80] Count Per Million normalization was computed on raw count matrices. Because the sequenced samples were of pooled myeloid subsets from five patients (N = 1 pool per myeloid subset), we computed further transformation to enable gene expression analyses. We used the innate immune samples as a reference transcriptome background to transform CPM values of the THBS1$^+$ myeloid pools. A geometric mean of the six innate immune samples was calculated as follows: exp(mean(log(x +1))). Then, for each of the THBS1$^+$ M pool and each feature, a ratio of (THBS1_M_CPM)/(innate Geometric Mean) was computed. Genes of interest including 'MDSC'-associated genes[27,28] and scRNAseq-specific markers were visualized on heatmap with a Log2 transformation. To further investigate the transcriptomic programs of the three THBS1$^+$ M pools, we did the following protocol independently for each THBS1$^+$ M pool: 1) *Z* score transformation, 2) fitting of *Z* score distribution, and 3) right-tailed p value estimation (over-expressed features). The fitting distribution allowed us to determine significantly over-expressed features in a pool. We selected genes with a p_value <0.01 to perform enrichment analyses using gprofiler on *Z* score ranked values.

QUANTIFICATION AND STATISTICAL ANALYSIS

Statistical analyses were performed with GraphPad Prism version 9 (GraphPad software) or R version 4.1. The statistical tests used are reported in the Figure Legends. n, represents the number of PBMC donors, HCC cases or mice and is reported in the Figure Legends. Cell abundance correlations were calculated using corrplot (version 0.92) and Hmisc (version 4.6.0) R packages. Correlation matrix was done using *cor* function with pearson method and corrplots were calculated using options order = "hclust". For each analysis, significant evaluation is reported in the Figure Legends. Data are presented as mean ± SEM unless otherwise indicated.